# *Interactive comment on* "Mobile MAX-DOAS observations of tropospheric $NO_2$ and HCHO during summer over the Three Rivers' Source region in China" *by* Siyang Cheng et al.: Authors' Response

We thank the editor for handing this manuscript and the two anonymous referees for their insightful comments and constructive suggestions on our manuscript. Below are our point-to-point responses to the comments from each referee. Also enclosed is the revised version of the manuscript, marked up using revision track. Note that the color schemes in Figures 8, 11, S7 have been adjusted in the revised manuscript which allow readers with color deficiencies to correctly interpret our findings, as suggested by the editorial support team.

# *Interactive comment on* "Mobile MAX-DOAS observations of tropospheric $NO_2$ and HCHO during summer over the Three Rivers' Source region in China" *by* Siyang Cheng et al.: Reply to Anonymous Referee #1

Referee comments are in black. Author responses are in blue.

Thanks to the authors for responding to the prior reviews. These were useful checks, but I think that these have led to some aspects that deserve further exploration. Specifically, the prior reviews requested that the authors check the geometric approximation using $O_4$ data, consider ground slope, further address the signal to noise of the observations, and consider comparisons to satellite observations. Below are some aspects of these issues that should be explored by the authors such that a revised manuscript can be made and re-considered for publication.

Reply: First of all, we appreciate the reviewer's comments on our manuscript. In response to the reviewer's comments and suggestions, we have made relevant revisions to the manuscript. Listed below are our responses and the corresponding changes made to the manuscript according to the suggestions given by the reviewer.

- Failure of geometric model to retrieve $O_4$ VCD:

The response to reviewers indicates that $O_4$ is not well retrieved by the geometric approximation using 15 ° elevation angle viewing geometry. The $O_4$ VCD retrieved using the geometric approximation is often half (~40 to 60%) of the column that is calculated from meteorological data. This is worrisome with respect to the quantification of VCDs by the geometric method. The authors have made a useful set of calculations using a radiative transfer model (RTM), which appears to show that this underrepresentation of $O_4$ is also in the RTM. The authors do not discuss why $O_4$ should fail but the geometric approximation should succeed for $NO_2$ and HCHO, despite their desire to keep using the geometric method for $NO_2$ and HCHO. The authors should explore for reasons why $O_4$ fails by the geometric method yet apparently succeeds for $NO_2$ and HCHO in order to keep using the geometric method for these gases.

One possible speculation could be that $O_4$ at larger heights above the surface is not contributing as much to the SCD as does $O_4$ nearer the surface. The scale height of $O_4$

is about 3.5km (half the scale height of pressure due to $O_4$ amount being proportional to the square of $O_2$). The table in the reply to reviewers indicates that $NO_2$ and HCHO are assumed to have a layer height of 0-1km or 0-2km (I presume above the terrain), so even with a 2km thick layer of these gases, most of the $O_4$ column is above the 2km top of these layers. If the geometric approximation is less sensitive to this higher-altitude part of the $O_4$ column, it might explain why the geometric approximation is failing for $O_4$. This hypothesis could be tested by splitting the $O_4$ distribution in the RTM into a below 2km (AGL) and an above 2km part and running the model on these two parts. Whether this idea proves out or not, the authors should explore and discuss reasons why the geometric approximation for $O_4$ failed yet they want to keep using it for $NO_2$ and HCHO.

Reply: As suggested by the reviewer, we performed additional RTM simulations. We considered the following scenarios:

a) $O_4$ profile with the concentration in the lowest 2 km set to zero

b) $O_4$ profile with the concentration above 2 km set to zero

c) HCHO background profile (Fig. S2) with the concentration in the lowest 2 km set to zero

d) $O_4$ profile with effects of clouds with an optical depth of 10 at different altitudes (2-3km, 4-5km, 8-9km)

e) Trace gas box profile from the surface to 2km with effects of clouds with an optical depth of 10 at different altitudes (2-3km, 4-5km, 8-9km)

The results are shown in the new figures S3 and S4, see below.

The main conclusions are:

1) the sensitivity of the geometric approximation for $O_4$ is high (~90%) for the part below 2km, but is low (~40%) for the part above 2km. This explains why the $O_4$ VCD retrieved using the geometric approximation is generally underestimating the true $O_4$ VCD.

2) the sensitivity of the geometric approximation for the part of the background HCHO above 2km is also low (~40%). Thus the use of the geometric approximation systematically underestimates the background HCHO above 2km. However, from model simulations over the Tibetan Plateau (Fig. S2), we find that the corresponding vertical HCHO column density is rather small: about $1.3\times10^{15}$ molec/cm$^2$. Thus the retrieved HCHO VCDs underestimate the true total VCD by about $0.6\times1.3\times10^{15}$ molec/cm$^2$ $\approx 8\times10^{14}$ molec/cm$^2$.

3) in the presence of clouds, the sensitivity for trace gases below the clouds is slightly enhanced compared to the geometric approximation, while it is strongly reduced for trace gases above the clouds. This finding confirms the assumption that clouds lead to a further underestimation of $O_4$ (and background HCHO) while the sensitivity for the trace gases close to the surface is almost unchanged.

An important reason to explore the failing of the geometric method for $O_4$ is that for smaller columns of HCHO, there is a larger contribution of "background" HCHO arising from oxidation of methane to the HCHO VCD. This "background" HCHO is not just in the boundary layer, but extends further aloft because methane is fairly well mixed in the troposphere. Therefore, the actual profile of HCHO might not be the assumed 0-1km or 0-2km layer, which succeeded in the geometric approximation retrieval, but might look more like that of $O_4$, and might therefore be underestimated by the geometric approximation (as O4 is). Figure S1 in the revised supplement may start to hint at increased underestimation of the true column for HCHO as the layer thickness increases from 0-1km to 0-2km. I believe that some satellite retrievals measure the differential VCD compared to a reference sector and then add back this "background" column of HCHO to get a total column. The "background" column typically comes from a global chemical transport model and examination of the column over this high-altitude region could give an estimate of the fraction of the HCHO column that is in the background (and thus potentially under-represented in the geometric retrieval). Figure S2 in the revised supplement indicates that HCHO's mixing ratio profile is much more constant with altitude than $NO_2$, which may indicate that the HCHO concentration profile extends to higher altitudes AGL than does the $NO_2$ profile, potentially indicating that the RTM calculations that assume HCHO is in the 0-1km (AGL) or 0-2km layer are not appropriate. The authors should explore how their geometric method would work for "background HCHO" and use satellite / GCM estimates of the background to determine how much of the columns they are observing may be not in the boundary layer.

Reply: Many thanks for this good suggestion! We made the corresponding RTM simulations (see also above) using a typical HCHO background profile (Fig. S2) from a GCM (Ma et al., 2019). We found that the sensitivity of the geometric approximation for the background HCHO above 2 km is only about 40%, leading to a systematic underestimation of the total HCHO VCD by about $8\times10^{14}$ molec/cm$^2$.

**Reference:**

Ma, J., Brühl, C., He, Q., Steil, B., Karydis, V. A., Klingmüller, K., Tost, H., Chen, B., Jin, Y., Liu, N., Xu, X., Yan, P., Zhou, X., Abdelrahman, K., Pozzer, A., and Lelieveld, J.: Modeling the aerosol chemical composition of the tropopause over the Tibetan

Plateau during the Asian summer monsoon, Atmospheric Chemistry and Physics, 19, 11587-11612, 10.5194/acp-19-11587-2019, 2019.

In the reply to reviewers, the authors say: "Part of the underestimation is probably related to clouds, but a strong underestimation is also found for measurements for clear skies." It would be useful to give more information on this statement. Specifically, there are times when the $O_4$ VCD is very small (e.g. on July 25, 2021) during a cloudy period? Can the authors indicate when there were clouds on their timeseries so that we can understand the effect of those clouds? Although the author's radiative transfer simulations can help to address questions of largely clear-sky behavior (they have AOD up to 0.2), the simulations do not help address understanding of cloudy behavior. It may be the case that if there is a cloud that is above the boundary layer $NO_2$ that the presence of the cloud might not affect the retrieval much, but the authors have not shown that. Can the authors expand the radiative transfer simulations to include a layer cloud aloft? That seems like a situation that should be addressable with their model.

Reply: Many thanks for your comments.

We performed additional RTM simulations for cloudy situations (clouds with an OD of 10 at different altitudes: 2-3km, 4-5km, 8-9km).

As expected, the sensitivity for the trace gases below the clouds is hardly affected (even slightly enhanced), but for trace gases above the cloud it is strongly reduced. These findings can explain the observed strong underestimation of the $O_4$ VCDs for some days.

It is a pity that we have no detailed information on the time series of clouds along the driving routes. We only qualitatively estimate the cloud conditions based on the observer manual recordings. As a whole, the weather conditions are dominated by the sunny sky and light rain or cloudy sky for the second and third circling journeys, respectively. And yes, it is cloudy on July 25, 2021.

Although the radiative transfer model calculations are useful, details on these calculations are lacking. For example, which radiative transfer model is used? Presumably some aerosol properties (e.g. asymmetry factor, single scattering albedo) are used, but are not stated. The $O_4$ simulations say 0-1000m in their caption box on the figure, which I guess is the aerosol layer thickness because $O_4$ goes a lot higher than that. Please clarify what this height range refers to.

Reply: We added the following information to the revised version of the paper:

-the Monte Carlo RTM MCARTIM was used for the simulations (see Deutschmann et al., 2011).

-the aerosol optical properties are: asymmetry parameter: 0.68, single scattering albedo: 0.95

-the cloud optical properties are: asymmetry parameter: 0.85, single scattering albedo: 1.0

-the altitude information in the figures describes the layer height of the aerosols, and for $NO_2$ and HCHO also the trace gas layer heights.

**Reference:**

Deutschmann, T., S. Beirle, U. Frieß, M. Grzegorski, C. Kern, L. Kritten, U. Platt, C. Prados-Román, J. Puķı̄te, T. Wagner, B. Werner, K. Pfeilsticker, The Monte Carlo atmospheric radiative transfer model McArtim: Introduction and validation of Jacobians and 3D features, Journal of Quantitative Spectroscopy and Radiative Transfer, Volume 112, Issue 6, 1119-1137, https://doi.org/10.1016/j.jqsrt.2010.12.009, 2011.

- Effect of ground slope:

The authors calculate that errors up to 21% can arise from slope, which is a good number to keep in mind. The authors then go on to average positive and negative slope errors to get a near zero error (1%). However, that calculation assumes equal mix of up and downhill driving, while in fact there might not be an equal mixture. Later they indicate that only about 1 minute in 8 minutes is observing at 15 °, so the slope during that period is what matters, and driving up or down a slope for a minute seems very reasonable in an area that covers ~3km vertical range. I think it would be safer to say that the ground slope may lead to an error of +/-21%, but that over the full loop these errors should at least partially cancel. It is possible that these errors might contribute to the low correlation between the mobile measurements and satellite observations.

Reply: Many thanks for your comments. The descriptions about the effect of the ground slope in the revised manuscript have been amended as: “The corresponding error of an individual measurement will be up to about 21%, but over the full loop

these errors will at least partially cancel.”.

In addition, although on the duration of the measurement at 15° elevation angle is only 1 min, we compared VCDs derived for different elevation angles (at different times of the same measurement sequence) and then the $VCD_{15°}$ were filtered based on the differences of VCDs between 15° and 20°, which can partially eliminate the VCDs with large errors when there are significant differences in ground slope between different elevation angles.

Yes, the errors will affect the correlation between the mobile measurements and satellite observations. However, for the comparison with TROPOMI observations, we use the means of typically 2-3 data points at a specific grid (0.25°×0.25°) in order to reduce the uncertainties of the VCDs from both mobile MAX-DOAS and TROPOMI.

- Error estimates:

Text was added to the end of section 3.1 describing error analysis. The authors appear to use two times the median spectral fit error. I presume the fit error is like a standard deviation (sigma), so this is 2*sigma, a reasonable definition of detection limit, but the text should be more clear. These (2-sigma) DL are 0.24×10^15 molecule cm^-2 for NO2 and 0.74×10^15 molecule cm^-2 for HCHO. These detection limit estimates use the airmass factor at 15°(e.g. the geometric approximation), but no error is added for uncertainties in the geometric approximation. I think that at least 21% error for road tilt and ~20% error from the radiative transfer calculations should be added to this spectroscopic-only error estimate.

Reply: Many thanks for your comments. During DOAS measurements, the detection limit can be conveniently estimated by the spectral fit errors (Cheng et al., 2021; Coburn et al., 2011; Stutz and Platt, 1996). We clearly stated the definition of the instrument detection limit in the revised manuscript, which is traceable for future references.

Due to the detection limit estimated from the medians of the DOAS fit errors over the full loop (including the conditions of driving up and down a slope), the error for the road tilt is probably much smaller than 21% and not the main error among the error sources of detection limit. Nevertheless, in the revised version of the manuscript,

we added the following sentence to mention the effects of the geometric approximation and the ground slope:

'Note that for individual measurements, the VCD detection limits might be lower or higher by about ±30% because of the uncertainties of the geometric approximation (up to about 20%) and the effect of varying ground slope (also up to about 20%).'

**Reference:**

Cheng, S., Ma, J., Zheng, X., Gu, M., Donner, S., Dörner, S., Zhang, W., Du, J., Li, X., Liang, Z., Lv, J., and Wagner, T.: Retrieval of $O_3$, $NO_2$, BrO and OClO Columns from Ground-Based Zenith Scattered Light DOAS Measurements in Summer and Autumn over the Northern Tibetan Plateau, Remote Sensing, 13, 4242, 10.3390/rs13214242, 2021.

Coburn, S., Dix, B., Sinreich, R., and Volkamer, R.: The CU ground MAX-DOAS instrument: characterization of RMS noise limitations and first measurements near Pensacola, FL of BrO, IO, and CHOCHO, Atmospheric Measurement Techniques, 4, 2421-2439, 10.5194/amt-4-2421-2011, 2011.

Stutz, J. and Platt, U.: Numerical analysis and estimation of the statistical error of differential optical absorption spectroscopy measurements with least-squares methods, Appl. Opt., 35, 6041-6053, 10.1364/AO.35.006041, 1996.

In section 4.1 (and the abstract), "background" levels of these gases are described, with an +/- listed (I would have assumed to be an error estimate), yet it is differently defined than the section 3.1 error analysis. In section 4.1, the text says "The uncertainties of the background levels were estimated by the half width at half maximum of Lorentz fitted curves (Fig. 6a)." I think that these are not "uncertainties", but rather the combination of variability in the species combined with analytical uncertainties in the measurements. The Lorentzian half width is used, which I think would be narrower than 1-sigma of a Gaussian fit. Can the authors justify why a Lorentzian is used here rather than a Gaussian? The Gaussian is connected to normal statistical error analysis and seems preferable, although the distributions do look longer tailed than a Gaussian. Overall, the similarity of section 3.1 detection limits and the width of the distributions in Figure 6 would lead me to believe that a significant part of the width of these distributions is instrumental noise. The quoting of the Lorenzian half width in the abstract seems misleading to me as I would have expected that the +/- number listed would be a Gaussian error estimate, possibly even

2-sigma. Please clarify this error discussion and make sure that the definition of the error estimate is included in the abstract.

Reply: Many thanks for your comments. The description about the background level and its uncertainties has been amended in the revised manuscript: "According to the Lorentz fitted curves of the relative frequency distribution of the $NO_2$ and HCHO VCDs during the field campaign (Fig. 6a), the background levels were 0.40 ± 1.13 $\times 10^{15}$ molec·cm$^{-2}$ for $NO_2$ and 2.27 ± 1.66 $\times 10^{15}$ molec·cm$^{-2}$ for HCHO in summer on the northeast of the Tibetan Plateau. Wherein the uncertainties of the background levels were estimated by the standard deviations of the $NO_2$ and HCHO VCDs". The corresponding revisions have been made in the sections of abstract and conclusions.

The purpose of curve fitting is to find the peaks of relative frequency distribution of the $NO_2$ and HCHO VCDs during the field campaign. The bigger relative frequencies are concentrated near the peak, meaning that the curve peak fitting should use the function with relatively narrow line width. Therefore, we prefer to use the Lorentz function, which fits the relative frequency distribution of the $NO_2$ and HCHO VCDs well in fact (Fig. 6a).

- Comparison to satellite:

The text says "Interestingly, there is almost no correlation of the two data sets, if we only use the tropospheric $NO_2$ VCDs within the 1.5 h time difference between mobile MAX-DOAS and TROPOMI at the same grid (referred to 'ΔT1.5' in Fig. 15a, corresponding to the red pluses in Fig. 13)." It seems to me that the noise on the measurements, both satellite and ground based, coupled with effects like slope, variable solar geometry, etc. are all going to reduce the correlation between the two data sets, particularly due to the low levels of these pollutants at these high-altitude remote sites. Therefore, I think the weak correlation is to be expected and is a product of the low level of pollution. Although the correlation is poor, the difference on average of the data by both methods (the bias) is a useful result of the study. I believe that the other reviewer also seeks to have greater focus on the bias in measurements than correlation (given noise on both measurements). The discussion of this correlation plot should include reference to the error estimates discussed above and also should discuss errors on TROPOMI measurements.

Reply: Many thanks for your comments. Yes, the weak correlation is to be

understandable: (1) The level and the range of variation of the $NO_2$ VCDs are very small in the background atmosphere over the Tibetan Plateau; (2) The signal-to-noise ratio is reduced due to the measurement errors for both MAX-DOAS (see section 3) and TROPOMI, introduced by the spectral analysis, ground slope, and the applied tropospheric AMF. The TROPOMI relative precisions in the '$\Delta T_{1.5}$' situation are estimated to be 72% and 113% for tropospheric $NO_2$ and HCHO VCDs, derived from the products of S5P_L2__NO2____HiR and S5P_L2__HCHO___HiR, respectively. These information has been added in the revised manuscript.

We have added the absolute differences (i.e. bias VCD values) in the revised manuscript. The varying mountainous terrain could lead to the horizontal inhomogeneity of the $NO_2$ and HCHO VCDs. The satellite measurements represent the averaged $NO_2$ and HCHO VCDs at a specific grid cell, while MAX-DOAS observations reflect the $NO_2$ and HCHO VCDs in a specific viewing direction. Therefore, one possible reason for the VCD bias between the two methods is the effect of mountainous terrain. However, without detailed knowledge about the true 3D $NO_2$ and HCHO distribution, this bias can not be fully understood in direction and magnitude. A corresponding description has been amended in the revised manuscript.

# *Interactive comment on* "Mobile MAX-DOAS observations of tropospheric $NO_2$ and HCHO during summer over the Three Rivers' Source region in China" *by* Siyang Cheng et al.: Reply to Anonymous Referee #2

Referee comments are in black. Author responses are in blue.

Reply: First of all, we appreciate the reviewer's positive comments on our manuscript. Listed below are our responses and the corresponding changes made to the manuscript according to the suggestions given by the reviewer.

DOAS detection limit is often defined based on the RMS noise than DOAS fit error (e.g. Stutz and Platt, 1996, Coburn et al., 2011). 1 σ RMS roughly corresponds to 3 σ DOAS fit error. The authors have conveniently decided to use 2 σ DOAS fit error as the detection limit which results in most the measurements being above the detection limit. The authors have clearly stated their definition of the detection limit so I think it is fine and traceable for future references.

Stutz, J. and Platt, U.: Numerical analysis and estimation of the statistical error of differential optical absorption spectroscopy measurements with least-squares methods, Appl. Opt., 35, 6041– 6053, doi:10.1364/AO.35.006041, 1996.

Coburn et al.: The CU ground MAX-DOAS instrument: characterization of RMS noise limitation and first measurements near Pensacola, FL of BrO, IO and CHOCHO.

Reply: Many thanks for your comments. With respect to the methods of obtaining the DOAS detection limit, the information above is important. We have added the two references (i.e. Stutz and Platt, 1996, Coburn et al., 2011) to the revised manuscript, so that the paper will be more readable and referable.

It is not clear how mountainous terrain would result in positive $NO_2$ and HCHO bias for TROPOMI. I suggest the authors also add bias VCD values in the paper along with the % bias.

Reply: Many thanks for your comments and suggestions.

The positive bias for '$\Delta T_{1.5}$' is probably related to horizontal $NO_2$ and HCHO inhomogeneities, caused by mountain terrains over the main area of the Three Rivers' Source. However, without detailed knowledge about the true 3D $NO_2$ and HCHO distribution, this bias can not be fully understood in direction and magnitude.

We have added the absolute differences (i.e. bias VCD values) in the revised manuscript.

# Mobile MAX-DOAS observations of tropospheric $NO_2$ and HCHO during summer over the Three Rivers' Source region in China

Siyang Cheng[1,2], Xinghong Cheng[1], Jianzhong Ma[1], Xiangde Xu[1], Wenqian Zhang[1], Jinguang Lv[2], Gang Bai[3], Bing Chen[4], Siying Ma[4], Steffen Dörner[5], Sebastian Donner[5], Thomas Wagner[5]

[1]State Key Laboratory of Severe Weather & Institute of Tibetan Plateau Meteorology, Chinese Academy of Meteorological Sciences, Beijing, 100081, China
[2]State Key Laboratory of Applied Optics, Changchun Institute of Optics, Fine Mechanics and Physics, Chinese Academy of Sciences, Changchun, 130033, China
[3]Beijing Remnant Technology Co.,Ltd, Beijing, 100012, China
[4]College of Electronic Engineering, Chengdu University of Information Technology, Chengdu, 610225, China
[5]Max Planck Institute for Chemistry, Mainz, D-55020, Germany

*Correspondence to*: Jianzhong Ma (majz@cma.gov.cn) and Xinghong Cheng (cxingh@cma.gov.cn)

**Abstract.** The tropospheric concentrations of nitrogen dioxide ($NO_2$) and formaldehyde (HCHO) have high spatio-temporal variability, and in situ observations of these trace gases are still scarce especially in remote background areas. We made four similar circling journeys of mobile MAX-DOAS measurements in the Three Rivers' Source region over the Tibetan Plateau in summer (18–30 July) 2021 for the first time. The differential slant column densities (DSCDs) of $NO_2$ and HCHO were retrieved from the measured spectra with very weak absorptions along the driving routes. The tropospheric $NO_2$ and HCHO vertical column densities (VCDs) were calculated from their DSCDs by the geometric approximation method, and they were further filtered to form reliable data sets by eliminating the influences of sunlight shelters and vehicle's vibration and bumpiness. The observational data show that the tropospheric $NO_2$ and HCHO VCDs decreased with the increasing altitude of the driving route, whose background levels ± standard deviations were 0.40 ± 1.13~~0.23~~ $\times 10^{15}$ molec $cm^{-2}$ for $NO_2$ and 2.27 ± 1.66~~0.96~~ $\times 10^{15}$ molec $cm^{-2}$ for HCHO in July 2021 over the Three Rivers' Source region. The $NO_2$ VCDs show similar geographical distribution patterns between the different circling journeys, but the levels of the HCHO VCDs are different between the different circling journeys. The elevated $NO_2$ VCDs along the driving routes were usually corresponding to enhanced transport emissions from the towns crossed. However, the spatial distributions of the HCHO VCDs depended significantly on natural and meteorological conditions, such as surface temperature. By comparing TROPOMI satellite products and mobile MAX-DOAS results, we found that TROPOMI $NO_2$ and HCHO VCDs have large positive offsets in the background atmosphere over the main area of the Three Rivers' Source. Our study provides valuable data sets and information of $NO_2$ and HCHO over the Tibetan Plateau, benefitting the scientific community in investigating the spatio-temporal evolution of atmospheric composition in the background atmosphere at high altitudes, validating and improving the satellite products over mountain terrains, and evaluating the model's ability in simulating atmospheric chemistry over the Tibetan Plateau.

## 1 Introduction

The Tibetan Plateau, also known as the Qinghai-Tibet Plateau in China, is usually called as "the Third Pole" (or "the Roof of the World") with an average surface altitude of 4000~5000 m, covering a vast region located at 73~105 °E longitude and 26~40 °N latitude (Qiu, 2008). Due to thermal and dynamic processes on the role of high altitude and large terrain, the Tibetan Plateau has an important influence on the atmospheric circulation (such as Asian Summer Monsoon), Asian climate and even global climate, and hydrological cycle (Bolin, 1950; Boos and Kuang, 2010; Dong et al., 2017; Duan et al., 2007; Liu et al., 2007; Yanai et al., 1992; Zhou et al., 2009). As the "Asian Water Towers", there are many water resources in the forms of glaciers, snow packs, lakes and rivers over the Tibetan Plateau, which is the headwaters of major rivers in Asia (such as Indus River, Ganges River, Yangtze River, Yellow River and Lancang River) and influences the economic development and billions of people survival in the downstream region (Xu et al., 2008; Gao et al., 2019). Therefore, the area of "Three Rivers' Source" (i.e. Yangtze River, Yellow River and Lancang River) was established as one of the first five national parks in China in 2021 to better protect the ecological environment. However, we still know very little about the ecological environment including atmospheric environment over this region at present. Almost no observations focus on the abundances and variations of atmospheric composition over the Three Rivers' Source region, limited by the extremely high altitude, topographical heterogeneity, variable weather, and effective techniques and methods. As one of the remote regions in Eurasia, the Tibetan Plateau with low anthropogenic activities and a low population density can be considered as natural laboratory to investigate the background atmospheric chemistry of the inner Eurasian continent (Ma et al., 2021). With increasing emissions of air pollution over the Tibetan Plateau and its surrounding areas (such as tourism in summer), measurements of the background atmosphere with high spatial-temporal resolution are urgent to improve the understanding of the spatio-temporal evolution of the atmospheric composition (Singh, 2021; Yang et al., 2019; Kang et al., 2022).

Nitrogen dioxide ($NO_2$) and formaldehyde (HCHO) are two important traces gases in the troposphere, participating in the control of the strong atmospheric oxidant of ozone ($O_3$) (Seinfeld and Pandis, 2016). Nitrogen oxides ($NO_x$), i.e. the sum of $NO_2$ and nitric oxide (NO), not only can be released by various anthropogenic emission sources, such as the burning of fossil fuel and biomass, but also can be emitted by natural processes including microbial activities in soils and lightning in the atmosphere (Lee et al., 1997; Granier et al., 2011; Kurokawa et al., 2013). HCHO is produced not only by primary sources (e.g. emissions of industry and transportation in city and biomass burning), but also by photochemical oxidation of methane and non-methane volatile organic compounds (e.g. isoprene emitted from natural vegetation) in the remote atmosphere (Stavrakou et al., 2009). High-accuracy measurements of $NO_2$ and HCHO with high spatial and temporal resolution are beneficial to understand their variation characteristics in the background atmosphere, quite useful to validate the satellite products, and very valuable to explore processes of atmospheric chemistry.

The ground-based observations of $NO_2$ and HCHO concentrations in the background atmosphere at high altitude are relatively scarce at present. Under the frameworks of the Global Atmosphere Watch program of the World Meteorological Organization (WMO/GAW) and the Network for the Detection of Atmospheric Composition Change (NDACC), long-term

observations of atmospheric composition have been carried out at some high mountain stations, such as the Waliguan (WLG; 3816 m above sea level) global atmosphere background observatory, located in the northeastern part of the Tibetan Plateau (Xu et al., 2020; Ma et al., 2021). With respect to $NO_2$ at WLG, previous studies found different levels (5~600 pmol·mol$^{-1}$) of $NO_2$ during different periods, leading to a positive or negative sign of net ozone production in the remote troposphere (Xue et al., 2011; Meng et al., 2010; Ma et al., 2020; Ma et al., 2002). Short-term HCHO observations at WLG in 2005 indicated that the possible sources for HCHO were photo-oxidation of biogenic emission of isoprene, animal excrement, and long-distance transportation from polluted air (Mu et al., 2007). The two stations of Qinghai Lake and Menyuan are adjacent to WLG, but the diurnal variations of $NO_x$ ($NO_2$) are different and possibly influenced by traffic and residential emissions, complex terrain, boundary layer processes, and transport from city air masses (Wang et al., 2015; Zhao et al., 2020). According to the measurements at the Qomolangma Atmospheric and Environmental Observation and Research Station (QOMS; 4276 m above sea level) of the south-central Tibetan Plateau from December 2017 to March 2019, the levels of $NO_2$ and HCHO were significantly higher than those at WLG station, related to local emissions (e.g. tourism, biomass burning, vegetation) and air pollution transport from the South Asia (Xing et al., 2021; Ma et al., 2020). Increased concentrations of tropospheric $NO_2$ at QOMS are concentrated in the lower layers with obvious seasonal variations (peak of 1.28 nmol·mol$^{-1}$ in autumn) and diurnal variations (two peaks at 11:00~13:00 BJT and after 16:00 BJT; BJT denotes Beijing Time and equals the Coordinated Universal Time plus 8 hours) (Xing et al., 2021). The tropospheric HCHO vertical distribution showed an exponential shape at QOMS with a seasonal peak of 5.20 nmol·mol$^{-1}$ in autumn, and the peaks of HCHO appeared between 10:00~16:00 BJT in winter and spring and after 16:00 BJT in summer and autumn, respectively (Xing et al., 2021). In recent years, the China National Environmental Monitoring Center (CNEMC) also established several atmospheric composition monitoring stations over the Tibetan Plateau, but they mainly focused on the continuous monitoring of the surface particulate matter with aerodynamic diameter less than 2.5 μm and 10 μm ($PM_{2.5}$ and $PM_{10}$), $NO_2$, sulphur dioxide ($SO_2$), $O_3$, and carbon oxide (CO) in cities, such as Lhasa and Xining (Chen et al., 2019; He et al., 2017; Yang et al., 2019). As a whole, these station observations cannot meet the demand of detecting the $NO_2$ and HCHO variations with high spatial resolution over the Tibetan Plateau, which are also crucial to the validation of satellite products over areas with complex terrain. To the best of our knowledge, there are no reports about mobile measurements of $NO_2$ and HCHO in the background atmosphere over the Tibetan Plateau.

The measurements of $NO_2$ and HCHO with high spatial and temporal resolution are challenging over the Tibetan Plateau. In the early days, some studies on $NO_2$ and HCHO were based on the time-consuming air sampling method (Mu et al., 2007; Meng et al., 2010; Ma et al., 2002). The air samplers were analysed by ion chromatography or a spectrophotometer for $NO_2$ and by a high-performance liquid chromatography and mass spectrometry or gas chromatography for HCHO in the laboratory. With the development of measurement techniques, in-situ methods started to be applied to measure surface concentrations of $NO_x$ ($NO_2$) and volatile organic compounds (VOCs) at a few stations (Wang et al., 2006; Xue et al., 2011; Wang et al., 2015; Zhao et al., 2020; Ran et al., 2014; Chen et al., 2019; Yang et al., 2019; Xue et al., 2013; Duo et al., 2018). These in-situ measurements at fixed stations were usually achieved by the chemiluminescence analyser for $NO_x$ ($NO_2$) and by the gas chromatography for VOCs, respectively. However, there are limitations in the spatio-temporal representation for the sampling

and in-situ measurement methods. As an alternative, satellite remote-sensing can perform long-term observations of $NO_2$ and HCHO and cover large areas with sparse spatio-temporal resolution, but the uncertainties of satellite $NO_2$ and HCHO products are rather large owing to complex terrain and weather over the Tibetan Plateau (Guo et al., 2016; Zhang et al., 2021). As a kind of advanced ground-based remote-sensing technique, Multi-AXis Differential Optical Absorption Spectroscopy (MAX-DOAS) has been certified in the measurement techniques of NDACC (Mazière et al., 2018). The successful observations of trace gases with very low abundances by MAX-DOAS depend on multi-factors, such as long optical paths, a high signal-to-noise ratio of the instrument, and characteristic spectral absorption features of the target species. According to previous studies, MAX-DOAS has the potential to measure tropospheric trace gases with very low level mixing ratios (pmol $mol^{-1}$ order for $NO_2$ and sub-nmol $mol^{-1}$ order for HCHO) in the background atmosphere at high altitude stations (Franco et al., 2015; Gil-Ojeda et al., 2015; Gomez et al., 2014; Marais et al., 2021; Schreier et al., 2016). Also, this technique has been used to measure the levels and monthly variations of $NO_2$ and HCHO in the global pristine atmosphere at WLG station (Ma et al., 2020). Stratospheric $O_3$ and its depleting substances (including $NO_2$) have been successfully retrieved from zenith DOAS spectra at a clean suburb station in the northern Tibetan Plateau (Cheng et al., 2021). Moreover, ground-based MAX-DOAS has been applied to monitor vertical distributions of $NO_2$ and HCHO in the southern Tibetan Plateau (Xing et al., 2021). Comparing with MAX-DOAS observation at a fixed site, mobile MAX-DOAS measurements in the background atmosphere over the Tibetan Plateau is a greater challenge, because: (1) Vehicle's violent vibration and bumpiness reduce the stability of the signal acquisition and even introduce unknown interference signals; (2) The measured signals can be strongly reduced by shelters due to complex terrain, such as tunnels, bridges, signposts, and mountains (usually such measurements have to be filtered out); and (3) The observations in practice are also controlled by various factors, e.g. variable weather, hypoxic environment in the plateau, geospatial signal loss and problems with the power supply. Although there are challenges in measuring $NO_2$ and HCHO concentrations by mobile MAX-DOAS over the Tibetan Plateau, they are useful for studies on the spatio-temporal evolution of the atmospheric composition in the background atmosphere, validation and improvement of satellite products over mountain terrain, and evaluation of the simulation results of atmospheric chemistry models over the Tibetan Plateau.

We made the mobile MAX-DOAS measurements in July 2021 over the plateau terrain for the first time. In this study, the primary objective is to analyse the spectra of scattered sun light collected in the Three Rivers' Source region over the Tibetan Plateau, obtain the data sets of tropospheric $NO_2$ and HCHO vertical column densities (VCDs) in the background atmosphere at high altitudes, and investigate the abundances and spatio-temporal variations of tropospheric $NO_2$ and HCHO VCDs during the field campaign. Large effort was spent on the spectral analysis and data filtering to obtain reliable tropospheric $NO_2$ and HCHO VCDs, because of the very weak spectral absorptions of the respective trace gases in the background atmosphere at high altitude as well as the influences of shelters and vehicle's vibration and bumpiness along the driving routes. In Section 2, we describe the field experiment in July 2021 over the Tibetan Plateau, including the observation vehicle, MAX-DOAS instrument, experiment region and deployment strategies. Section 3 introduces the spectral analysis as well as the calculation and filtering of the $NO_2$ and HCHO VCDs. In Section 4, we present the abundances, the spatio-temporal variation of the

tropospheric $NO_2$ and HCHO VCDs during the field campaign, as well as the comparison with TROPOMI products. Summary and conclusions are given in Section 5.

## 2 Field experiment

### 2.1 Description of vehicle and instrumentation

A mobile vehicle has been designed and assembled for measurements of atmospheric composition over the Tibetan Plateau (Fig. 1a). The mobile vehicle has been operated by the Chinese Academy of Meteorological Sciences (CAMS) since February 2021. The outside parts of instrumentation are fixed on the roof of the vehicle, which is about 3.5 m above the ground. The outside parts of instrumentation contain the sensors for spatial position (longitude, latitude, altitude) and attitude (yaw, pitch and roll angles) of the mobile vehicle. The units of the system control, data collection, screen display and Uninterruptible Power Supply (UPS) are mounted in the interior of the mobile vehicle. The UPS's battery pack, recharged after the mobile vehicle reaches the destination of observation route, can offer operation time of around 16 h with a power of 2000 W. All instrumentations have been specially reinforced to allow the mobile vehicle to travel over the difficult road conditions of the Tibetan Plateau. The mobile vehicle usually runs at a speed of ~60 km/h for motorways and ~40 km/h for ordinary roads, respectively, during our field experiment.

For the field campaign of mobile observations of the atmospheric environment over the Tibetan Plateau, the aforementioned vehicle was equipped with an instrument called Tube MAX-DOAS (Donner, 2016; Cheng et al., 2021), developed by the Max Planck Institute for Chemistry (MPIC), Mainz, Germany. The Tube MAX-DOAS contained two parts, one outside (Fig. 1b) and another inside (Fig. 1c) the vehicle, respectively. (1) The outside part was fixed on the rear of the vehicle's roof and is mainly composed of the telescope, optical fibre, stepper motor, tubular shell, and protective cover. The telescope, pointing to the back of the vehicle, rotated in the vertical plane to achieve the measurement at seven different elevation angles (3°, 6°, 10°, 15°, 20°, 30°, 90° relative to the mobile vehicle) driven by the stepper motor. The scattered sunlight was collected by the telescope and transferred to a spectrograph inside the vehicle via the optical fibre. (2) The inside part was made up of the spectrograph, data collection unit, temperature control unit as well as a laptop which controls the instrument operation and data collection. For each elevation angle, the Tube MAX-DOAS collected one spectrum at a stable detector temperature of 15 ± 0.1 ℃ with the integration time of ~1 min. The AvaSpec-ULS2048x64-USB2 spectrograph was built by the AVANTES company and covered the wavelength range of 300~466 nm with ~0.6 nm spectral resolution. The Tube MAX-DOAS not only automatically collected the scattered sunlight spectra for the cyclic elevation angle sequences during daytime, but also recorded spectra of dark current (DC) and electronic offset (OS) at night for correcting the daytime spectra of scattered sun light. The laptop coordinated the operation of each module during the measurement procedure. The MPIC Tube MAX-DOAS system has been successfully applied to the ground-based observations of atmospheric composition at the Golmud station over the northern Tibetan Plateau (Cheng et al., 2021).

### 2.2 Description of the measurement location and deployment strategies

The mobile field observation campaign was performed over the Three Rivers' Source region on the northeast of the Tibetan Plateau in western China (Fig. 2). The main vegetation types are alpine steppe and meadows in the region along the observation route, belonging to a unique and typical alpine ecosystem. The main landform is the mountain plain. The Three Rivers' Source region has a typical plateau continental climate, characterized by a large diurnal temperature difference, long sunshine time and strong solar radiation. There are also rapid spatial and temporal variations of the local climate over the Three Rivers' Source region. Yak and sheep grazing in summer is the main industry over the Three Rivers' Source region, isolated from industrial and population centres.

In order to reveal the background abundance and spatio-temporal variation of the atmospheric composition over the Three Rivers' Source region, we took various factors into consideration during the design of the deployment strategies, such as the regional representativeness of the driving routes, the technical requirement of the passive MAX-DOAS measurement, the sunlight shelter and the bumpy condition along the driving route, the reliable electric power safeguard, and first aid for sudden altitude sickness. Finally, the mobile MAX-DOAS field experiment was carried out in the southeast of Qinghai province, China (Fig. 2b). The driving routes traverse the Yangtze River and the Yellow River and are close to the Lancang River. It took three days for one circling journey. Four circling journeys were made during the mobile MAX-DOAS field experiment period in July 2021 (Table 1). We drove from the meteorological bureau of Xining city, the capital of Qinghai province, to the meteorological bureau of Dari county of the Guoluo Tibetan autonomous prefecture, south-eastern Qinghai province, on the first day of each circling journey (Fig. 2). We travelled from the meteorological bureau of Dari county to the meteorological bureau of the Yushu Tibetan autonomous prefecture on the middle day (Fig. 2). We returned to Xining city from the Yushu Tibetan autonomous prefecture on the third day (Fig. 2). Hereafter the three segments of the closed-loop journey are referred to as XD, DY, YX, respectively. The durations were about 12 h, 8 h, and 13 h for the XD, DY, and YX segments, respectively. Most of driving routes are motorways, except parts of the national roads in the YX segment. More sunlight shelters occurred in the XD segment, because of the tunnels, bridges, signposts, and mountains. The observed MAX-DOAS data were saved in the laptop, and backed up when arriving at the terminus of each segment of the journey. In addition to troubleshooting by field observers, our MAX-DOAS team also provided the technical support via remote wireless network during the campaign.

## 3 Spectral retrieval and data filtering

### 3.1 Spectral analysis

Based on the Beer-Lambert law, the column densities of trace gases can be retrieved from the scattered sunlight spectra by the widely used method of Differential optical absorption spectroscopy (DOAS) (Platt and Stutz, 2008). The basic idea of DOAS is to decompose the atmospheric spectral extinction into two terms, i.e. terms with slow spectral variation (such as atmospheric scattering) and fast variation (mainly trace gas absorptions) with wavelength. The slant column density (SCD) of a trace gas

is defined as its concentration integrated along the effective light path (Cheng et al., 2019). The total (from the instrument to the top of atmosphere) SCD can be split into two parts, i.e. so-called tropospheric SCD ($SCD_{Trop}$) and stratospheric SCD ($SCD_{Stra}$). For species concentrated in the troposphere or light traversing the same path in the stratosphere for different elevation angles ($\alpha$), the $SCD_{Stra}$ can be neglected or cancels out respectively, which means $SCD_{\alpha, Stra} \approx SCD_{90, Stra}$ (Ma et al., 2013). In the practice of the MAX-DOAS spectral analysis, a Fraunhofer reference spectrum (FRS) needs to be selected to correct the strong solar Fraunhofer lines. Thus the result of the spectral analysis is the so-called differential slant column density (DSCD) of the target species (such as $NO_2$ and HCHO in this study), which represents the difference in trace gas absorption between the measured atmospheric spectrum and the FRS (Hönninger et al., 2004). There are two schemes for the FRS selection from measured spectra (Wang et al., 2018): one is using a fixed spectrum (hereafter named "fixed FRS"), usually at the 90°elevation angle during noon to minimize the tropospheric and stratospheric contributions, for all measured spectra; the other is using sequential spectra (hereafter named "sequential FRS"), which are defined as the time interpolated spectra between two zenith spectra measured before and after the measurement time of the current off-zenith elevation angle. Due to more similar atmospheric conditions and instrument properties between a specific measured spectrum and the corresponding sequential FRS, higher signal-to-noise ratios and smaller fitting errors are achieved by using a sequential FRS than a fixed FRS. Fig. 3 shows the root mean square (RMS) of the spectral fitting residuals using a fixed FRS and sequential FRS for $NO_2$ and HCHO, respectively. It is clear that the RMS medians are smaller for using a sequential FRS than that for a fixed FRS. Thus we prefer to use the sequential FRS for the mobile MAX-DOAS measurement in this study. For $NO_2$, we can retrieve the DSCD not only in the ultraviolet (UV) region (351~390 nm) but also in the visible region (400~434 nm) (Cheng et al., 2022; Cheng et al., 2019). Fig. 4 compares the $NO_2$ DSCDs and the RMSs of the spectral fitting residuals for using either the visible and UV spectral interval. The overall trends of the $NO_2$ DSCDs are consistent between both spectral intervals with the correlation coefficient of R=0.75, but the averaged RMSs of the spectral fitting residuals in the visible wavelength region, i.e. $(6.26 \pm 6.92)\times10^{-4}$, are smaller than those in the UV wavelength interval, i.e. $(7.62 \pm 9.17)\times10^{-4}$. The final settings of the $NO_2$ and HCHO spectral retrieval parameters, such as cross sections of the target and interference species, Ring spectra, polynomial degree and intensity offset, similar as in previous studies (Cheng et al., 2022; Cheng et al., 2019), see Table 2. The spectral analysis, including DC and OS corrections of the measurement spectra and the spectral calibration of the FRS, was implemented by the QDOAS software based on a non-linear least squares fitting method, developed by the Royal Belgian Institute for Space Aeronomy (BIRA-IASB) (Danckaert et al., 2017). Fig. 5 shows an example of the spectral fitting for the $NO_2$ and HCHO DSCDs from a spectrum measured at the elevation angle of 15° at 11:02 BJT on 18 July 2021 (SZA = 34.11°). In the post processing of $NO_2$ and HCHO DSCDs, we applied the following filters: RMS < 0.005; offset (constant) should be between ± 0.03; SZA < 80 °. These filters were selected as they provide a good balance between quality of the results and skipping not too many data. These filters almost filtered out all "bad measurements", which were caused by sunlight shelters and bumpy conditions. Finally, relative to measurements with SZA<90 °, the percentages of remaining DSCD data were 69% for $NO_2$ and 74% for HCHO, respectively. During DOAS measurements, the instrument detection limit can be conveniently

estimated by the spectral fit errors (Cheng et al., 2021; Coburn et al., 2011; Stutz and Platt, 1996). ~~We estimated t~~The instrument detection limits of $NO_2$ and HCHO DSCDs were defined as~~to be~~ twice the medians of the spectral fit errors ~~(Cheng et al., 2021)~~in this study, i.e., $0.68\times10^{15}$ molec $cm^{-2}$ and $2.11\times10^{15}$ molec $cm^{-2}$ at 15 °elevation angle respectively. According to the DSCD detection limits divided by the differential air mass factor (DAMF) for 15 °elevation angle, the VCD detection limits were estimated to be about $0.24\times10^{15}$ for $NO_2$ and $0.74\times10^{15}$ for HCHO, respectively. Note that for individual measurements, the VCD detection limits might be lower or higher by about ±30% because of the uncertainties of the geometric approximation (up to about 20%) and the effect of varying ground slope (also up to about 20%). There are 17% and 15% of the retrieved $NO_2$ and HCHO DSCDs below the detection limits, respectively. Based on the spectral fit errors, we can also calculate the relative errors for each $NO_2$ and HCHO DSCD. Then the mean relative errors of $NO_2$ and HCHO DSCDs were about 21% and 12% at 15 °elevation angle, respectively.

### 3.2 $NO_2$ and HCHO VCDs

Based on the aforementioned filtered $NO_2$ and HCHO DSCDs retrieved from the spectra, we need to firstly obtain the tropospheric DSCDs at the elevation angle $\alpha$ (i.e., $DSCD_{\alpha,Trop}\equiv SCD_{\alpha,Trop}-SCD_{90,Trop}$), which are used to calculate the $NO_2$ and HCHO vertical column densities (VCDs) in the troposphere. In the situation of fixed FRS, the $DSCD_{Trop}$ are produced by the DSCDs of off-zenith viewing direction minus that at 90 °elevation angle of the same elevation sequence; In the case of sequential FRS in this study, the DSCDs from spectral inversion can be regarded as $DSCD_{Trop}$ (Hönninger et al., 2004).

The SCDs (or DSCDs) depend on the concentration profile of target species, effective light path length, measurement geometry and solar position. Using the air mass factor (AMF), the SCDs (or DSCDs) can be converted to the VCDs, which are independent of the light path and the observation geometry and thus convenient for comparison between different measurements. The tropospheric AMF at the elevation angle $\alpha$ ($AMF_{\alpha,Trop}$) is given by the ratio of the SCD to VCD in the troposphere:

$$\mathrm{AMF}_{\alpha,\mathrm{Trop}} = \frac{\mathrm{SCD}_{\alpha,\mathrm{Trop}}}{\mathrm{VCD}_{\mathrm{Trop}}} \quad (1)$$

If $\alpha = 90^{\circ}$,

$$\mathrm{AMF}_{90,\mathrm{Trop}} = \frac{\mathrm{SCD}_{90,\mathrm{Trop}}}{\mathrm{VCD}_{\mathrm{Trop}}} \quad (2)$$

We define the $DAMF_{\alpha,Trop}$ as the tropospheric differential AMF, i.e.

$$\mathrm{DAMF}_{\alpha,\mathrm{Trop}} = \mathrm{AMF}_{\alpha,\mathrm{Trop}} - \mathrm{AMF}_{90,\mathrm{Trop}} \quad (3)$$

By equation (1) minus equation (2), $VCD_{Trop}$ can be deduced:

$$\mathrm{VCD}_{\mathrm{Trop}} = \frac{\mathrm{SCD}_{\alpha,\mathrm{Trop}}-\mathrm{SCD}_{90,\mathrm{Trop}}}{\mathrm{AMF}_{\alpha,\mathrm{Trop}}-\mathrm{AMF}_{90,\mathrm{Trop}}} = \frac{\mathrm{DSCD}_{\alpha,\mathrm{Trop}}}{\mathrm{DAMF}_{\alpha,\mathrm{Trop}}} \quad (4)$$

where the AMF can be simulated by an atmospheric radiative transfer model or estimated by the method of geometric approximation. The former method is more accurate, but requires information on various input parameters, such as the profiles

of trace gas and aerosol, which are usually not known. The latter method is simpler and assumes trace gases are uniformly distributed in the lower troposphere. Due to the lack of necessary data over the Tibetan Plateau to simulate the correct $NO_2$ and HCHO AMFs, we adopted the geometric approximation method in this study. Here it should be noted that the errors caused by the geometric approximation method are much smaller for measurements at high altitudes, because the scattering probability is much smaller compared to measurements at sea level. Thus the direct viewing path length becomes longer and is in better agreement with the assumptions of the geometric approximation method. We explored the applicability of the geometric approximation method by radiative transfer simulations with the full spherical Monte Carlo radiative transfer model MCARTIM (Deutschmann et al., 2011) (see Section S1). The main findings are: (1) ~~For typical trace gas and aerosol profiles, the~~The typical errors of the geometric approximation are <20% for $NO_2$ and HCHO (~~see Sect~~Fig. S1)~~.~~; (2) The retrieved HCHO VCDs using the geometric approximation will well represent the part of the HCHO profile located below 2km, but the use of the geometric approximation systematically underestimates (~60%) the background HCHO above 2km (Fig. S2, S3). However, from model simulations over the Tibetan Plateau (Fig. S2) (Ma et al., 2019), we find that the corresponding vertical HCHO column density is rather small: about $1.3\times10^{15}$ molec $cm^{-2}$. Thus the retrieved HCHO VCDs underestimate the true total VCD by about $0.6\times1.3\times10^{15}$ molec $cm^{-2}$= $8\times10^{14}$ molec $cm^{-2}$; (3) In the presence of clouds, the sensitivity for trace gases below the clouds is slightly enhanced compared to the geometric approximation, while it is strongly reduced for trace gases above the clouds (Fig. S4). The $AMF_{\alpha,Trop}$ in the condition of geometric approximation in polluted environment can be expressed as:

$$AMF_{\alpha,Trop} \approx \frac{1}{\sin(\alpha)} = \sin^{-1}(\alpha) \quad (5)$$

Therefore, equation (4) becomes

$$VCD_{Trop} = \frac{DSCD_{\alpha,Trop}}{\sin^{-1}(\alpha)-1}, (\alpha \neq 90^{\circ}, AMF_{90,Trop} = 1) \quad (6)$$

Ideally, the elevation angles should be corrected by the attitude angles of the mobile vehicle when applying the geometric approximation. However, the partial system of the attitude angles of the mobile vehicle did not work well, which may be connected with the special environment of Tibetan Plateau (such as low atmospheric pressure) and bumpiness of the mobile observation platform (leading to instabilities of the data collection). Thus we use the uncorrected elevation angles during the conversion of DSCD to VCD in equation (6). Of course, the uncorrected elevation angles will cause some errors if the mobile observation vehicle is not on a horizontal surface, but ~~on average these errors will partly cancel out. Also~~ these errors are typically small for the larger elevation angles (for example, $15^{\circ}$, $20^{\circ}$, $30^{\circ}$)~~ and can be neglected when compared to other uncertainties~~. Based on the mobile platform attitude angles, the elevation angle error is estimated to be about 2.3°. The corresponding error of an individual measurement will be up to about 21%, but over the full loop these errors will at least partially cancel. ~~However, it should be noted that on average the positive and negative deviations of the elevation angle will almost cancel each other. Thus the errors of individual measurements will be usually much smaller (except for measurements on continuous strong slopes). For averages of several measurements the errors of the elevation angles lead to much smaller VCD errors with a magnitude smaller than 1% when using geometric approximation method.~~ To further judge how good the geometric approximation is, the resulting VCDs derived for different elevation angles have been compared (Brinksma et al.,

2008). Table 3 shows the $NO_2$ (HCHO) VCDs between the three elevation angles ($15^\circ$, $20^\circ$, $30^\circ$). The VCDs are rather consistent at the three elevation angles with correlation coefficients of R=0.91–0.95 for $NO_2$ and R=0.66–0.80 for HCHO, respectively (Table 3). This implies that the geometric approximation method is self-consistent. The standard deviation of the $NO_2$ (HCHO) VCDs is small at $15^\circ$ elevation angles (Table 3), implying the high reliability of VCDs at $15^\circ$ elevation angle ($VCD_{15^\circ}$). Therefore, to compromise between accuracy of the geometric approximation and signal to noise, the $VCD_{15^\circ}$ were treated as the reliable results on a selection criterion (for $NO_2$, the absolute difference of VCDs between 15° and 20° is < $1\times10^{15}$ molec $cm^{-2}$ or the relative difference is <5%; for HCHO, the absolute difference of VCDs between 15° and 20° is < $2\times10^{15}$ molec $cm^{-2}$ or the relative difference is <5%). The filtered $NO_2$ and HCHO $VCD_{15^\circ}$ during the mobile measurement period were kept as the final results to explore the background abundance and spatio-temporal variation of $NO_2$ and HCHO over the Three Rivers' Source region of the Tibetan Plateau. It spent about 8 min for measurements at two adjacent 15° elevation angle. Therefore, the corresponding spatial resolution was approximately 8 km at a speed of ~60 km/h of the mobile vehicle. Assuming that the trace gas is located in the lowest 1000 m above the surface, we can also estimate the horizontal extent of the line of sight through that layer. For measurements at 15° elevation angle, this extent is about 4 km.

From our experience during the measurements, we also suggest that the telescope scans at $15^\circ$, $20^\circ$, $90^\circ$ elevation angles in future mobile MAX-DOAS measurements of the background atmosphere over mountain terrain. There are at least two reasons: (1) The relatively large elevation angles are less influenced by the road tilt and obstructions; (2) The measurements at 15° and 20° elevation angles have still an enhanced sensitivity to tropospheric trace gases (increase of sensitivity compared to 90° elevation angle is about a factor 3.8 and 2.9, respectively).

## 4 Interpretation of the results

### 4.1 Abundance

~~Based on filtered final $NO_2$ and HCHO VCDs, the means ± standard deviations were 0.69 ± 1.13 $\times10^{15}$ molec $cm^{-2}$ for $NO_2$ and 2.43 ± 1.66 $\times10^{15}$ molec $cm^{-2}$ for HCHO in July 2021 along the driving routes.~~ The background levels of the filtered final $NO_2$ and HCHO VCDs can be estimated by the maximum frequency method (Cheng et al., 2017). According to the Lorentz fitted curves of the relative frequency distribution of the $NO_2$ and HCHO VCDs during the field campaign (Fig. 6a), the background levels were 0.40 ± ~~0.23~~1.13 $\times10^{15}$ molec $cm^{-2}$ for $NO_2$ and 2.27 ± ~~0.96~~1.66 $\times10^{15}$ molec $cm^{-2}$ for HCHO in summer on the northeast of the Tibetan Plateau. ~~The~~ Wherein the uncertainties of the background levels were estimated by the ~~half-width at half-maximum of Lorentz fitted curves~~standard deviations of $NO_2$ and HCHO VCDs ~~(Fig. 6a)~~. The background levels are smaller than those observed in summer 2018 at the Qomolangma Atmospheric and Environmental Observation and Research Station of the Chinese Academy of Sciences, located in the south-central Tibetan Plateau (medians of 0.80 $\times10^{15}$ molec $cm^{-2}$ for $NO_2$ and 3.13 $\times10^{15}$ molec $cm^{-2}$ for HCHO, respectively) (Xing et al., 2021). To explore the dependence of the $NO_2$ and HCHO VCDs on the route altitude (in the range of 2280~4830 m), we divided the mobile route altitudes into

vertical bins with intervals of 500 m. Fig. 6b shows the means, medians and standard deviations of the $NO_2$ and HCHO VCDs in each vertical grid cell. There are generally decreasing trends with increasing altitude. This is consistent with our knowledge of the natural background atmosphere, i.e. the higher the altitude, the lower the air density. Different from the nearly constant decreasing rate of the HCHO VCDs with the route altitude, there are at least two segments with significantly different decreasing rates above and below 2750 m altitude. The $NO_2$ VCDs in the 2000~2500 m grid cell (8.17 $\times 10^{15}$ molec $cm^{-2}$) were substantially larger because the mobile route was close to the city of Xining (about 2260 m altitude), where there are stronger anthropogenic emission sources of air pollutants, such as increased urban transport emissions leading to higher $NO_2$ levels. The $NO_2$ VCDs were quite low in the altitude above 3500 m, partly related to almost no human activities at this altitude. Due to very limited emissions of anthropogenic VOCs over the Tibetan Plateau, the changes of the HCHO VCDs with altitude were likely to be primarily connected with the natural process, such as the oxidation of methane and non-methane volatile organic compounds (Stavrakou et al., 2009). Combining the hourly surface air pressure and temperature at 2 m above the land surface with the 0.25 °×0.25 °resolution from ERA5, the profiles of $NO_2$ and HCHO mixing ratios were also derived from the corresponding mean and median VCDs along driving routes, respectively (Fig. ~~S2~~S5). As a whole, the measurements (except close to the cities) at the higher altitudes in summer are able to reflect the background atmosphere with rather low $NO_2$ and HCHO levels over the Three Rivers' Source region.

### 4.2 Spatio-temporal variation

#### 4.2.1 $NO_2$

The day-to-day variations of $NO_2$ VCDs are similar between different circling journeys, characterized by the larger means and 90th percentiles on the first and the third days (i.e. on the days of the XD and YX driving routes) and correspondingly lower values on the second day (i.e. on the day of the DY driving route) of each circling journey (Fig. 7a). The $NO_2$ means are always larger than the medians on each day, especially in the situation of the XD driving route, partly because the driving route covers small areas with very high $NO_2$ abundances, such as Xining city, and large background areas with relatively low $NO_2$ abundances in the XD driving route. For the same driving route of the four circling journeys, the daily $NO_2$ levels are close to each other, with the $NO_2$ medians in the range of 0.19–0.63 $\times 10^{15}$ molec $cm^{-2}$ during the field campaign.

Figure 8 shows the spatial distributions of the tropospheric $NO_2$ VCDs along the XD, DY, and YX driving routes in July 2021. For the same segment of four circling journeys (i.e. XD, DY, or YX), the tropospheric $NO_2$ VCDs present a nearly consistent spatial distribution. It is also clear that the tropospheric $NO_2$ VCDs were elevated when the mobile observation vehicle passed through counties or cities, such as Xining and Yushu. This can be attributed to increased anthropogenic activities in cities or counties, such as traffic and residential emissions. There are significantly larger $NO_2$ VCDs on the driving routes of south-eastern Qinghai Lake, which is a famous tourist destination. Moreover, as one of the arterial roads to Tibet, there are many diesel vehicles passing through the basin of Qinghai Lake via national highways surrounding the lake. The touring buses or cars as well as the cargo transport vehicles could lead to the higher $NO_2$ abundances in summer around the Qinghai Lake.

According to previous studies at the northwest section of the Qinghai Lake shore in October of 2010 and 2011, the emissions from diesel vehicles around Qinghai Lake were likely the main source of nitrogen oxides ($NO_x$) (Wang et al., 2015). The enhanced $NO_2$ levels could even be found at the highway junction (such as the location of 98.97 °E, 35.20 °N) and the tunnel exit (such as the location of 99.40 °E, 34.92 °N; Note: The telescope of the MAX-DOAS pointed to the backward of the driving direction) (Fig. 8a1, d1). This situation would not appear once traffic flow was lower at these special locations (Fig. 8b1, c1). The $NO_2$ spatial distributions over the main area of the Three Rivers' Source, such as around the counties of Dari, Shiqu, Chenduo, and Maduo during the DY driving route and the first half of the YX driving route, were relatively uniform with very low levels ($<1\times10^{15}$ molec $cm^{-2}$). Previous investigations of the tropospheric ozone chemical budget, simulated and constrained by measured $NO_2$ concentration at the Waliguan background station located in the north-eastern Tibetan Plateau, showed that the $NO_x$ levels play the vital role in the net sign of ozone production from formation and loss reaction for the tropospheric background atmosphere (Ma et al., 2002; Ma et al., 2020; Xue et al., 2013). Therefore, with the more and more anthropogenic activities, the effects of increasing $NO_2$ levels on the photochemistry and oxidation capacity of the background atmosphere should be paid more attention to better build an ecological civilization over the remote Three Rivers' Source region in the future.

The available time period, confined by the sunshine duration and the distance of the driving routes, is the shortest for the DY driving route. The diurnal cycle of the $NO_2$ VCD means or medians presents high values in the morning and evening and shows lower levels of ~0.38 $\times10^{15}$ molec $cm^{-2}$ from 12:00 BJT to 17:00 BJT (Fig. 9a). The means of the $NO_2$ VCD are also significantly higher than the corresponding medians before 11:00 BJT with larger standard deviations. The $NO_2$ diurnal variation patterns of the XD, DY, and YX driving routes are different, although the diurnal patterns are rather consistent for different days of the same driving route (Fig. 9b-d). The $NO_2$ VCDs sharply decreased in the morning during the XD driving route, with larger standard deviations around 16:00 BJT, when the mobile observation vehicle was close to the toll station. For the DY driving route, the $NO_2$ VCDs stayed at the lower level and then slightly increased in the late afternoon. In the situation of the YX driving route, the diurnal pattern of $NO_2$ VCDs was a symmetric "U" shape. It should be noted that the mobile observation vehicle reached the destination of the YX driving route around 22:00 BJT and the lacking $NO_2$ VCDs were due to SZA > 80 ° after 20:00 BJT. The amplitudes of the $NO_2$ diurnal variation as well as the maxima $NO_2$ level among different driving routes were decreasing in the order of the segments XD, YX, and DY. Previous studies at the background station of lower altitude showed that the $NO_2$ diurnal variation could be affected by the higher photolysis rate owing to stronger solar irradiance at noon and for a site location far away from emission sources (Cheng et al., 2019). We also checked whether the enhanced $NO_2$ VCDs in the morning and evening might be an artefact caused by the effect of stratospheric $NO_2$ on the derived tropospheric $NO_2$ VCD. –In our data analysis (see section 3.1) it is assumed that the stratospheric $NO_2$ absorption is independent on the elevation angle. While this is not exactly true, it is a valid assumption for typical measurement situations in polluted or slightly polluted environments. If, however, the tropospheric $NO_2$ absorption is very weak, the remaining stratospheric influence might be substantial. We tested this potential influence of the stratospheric $NO_2$ absorption on the retrieved tropospheric $NO_2$ VCD for our measurements, by performing radiative transfer simulations using a stratospheric $NO_2$

profile with a stratospheric $NO_2$ VCD of 4 $\times 10^{15}$ molec $cm^{-2}$. As a result, we found that for SZA < 80 ° the introduced $NO_2$ DSCD for an elevation angle of 15 ° is < 1 $\times 10^{15}$ molec $cm^{-2}$ (see Fig. ~~S3~~S6) thus leading to a maximum artificial $NO_2$ VCD of 3.5 $\times 10^{14}$ molec $cm^{-2}$. Moreover, for SZA<80 °, the artificial $NO_2$ VCD shows almost no SZA dependence. Thus the potential influence of the stratospheric $NO_2$ absorption cannot explain the observed diurnal cycle of the tropospheric $NO_2$ VCD. From these findings we conclude that the $NO_2$ diurnal variations were primarily caused by enhanced pollution in the morning and evening when the mobile observation vehicle was located in or close to the cities or county town, i.e. the $NO_2$ diurnal patterns reflected the differences of the $NO_2$ spatial distribution. An additional effect on the diurnal variation is probably caused by the enhanced $NO_2$ photolysis around noon.

#### 4.2.2 HCHO

The means and medians of the daily HCHO VCDs are basically consistent on all days, with the maximum mean of 4.63 $\times 10^{15}$ molec $cm^{-2}$ on 21 July 2021 and the minimum mean of 1.15 $\times 10^{15}$ molec $cm^{-2}$ on 27 July 2021 (Fig. 7b). There are obvious differences in the levels of HCHO VCDs between the different circling journeys. The higher and lower HCHO VCDs appeared during the second circling journey (i.e. 21-23 July 2021) and the third circling journey (i.e. 25-27 July 2021), respectively. HCHO has large natural vegetation sources, with the emission strength depending strongly on weather conditions such temperature and solar radiation at the Earth's surface (Borovski et al., 2014). We looked at air temperature at 2 m above the land surface and the downward solar radiation at the surface (SSRD), which are derived from hourly ERA5 reanalysis data with 0.25 °×0.25 ° resolution. According to the ERA5 grid cell and hour to which each HCHO measurement belongs, the air temperature and SSRD are extracted and then averaged for each day (Fig. 10a). It is shown that the daily variations between air temperature and HCHO VCDs are highly correlated, with the correlation coefficient of R=0.95 (Fig. 7b, 10b). Probably higher temperatures are connected with more VOCs emitted by vegetation, leading to higher HCHO VCDs. The daily HCHO VCDs are also related to surface solar radiation, but with a smaller correlation coefficient of R=0.27 (Fig. 10b), which is probably caused by the higher variability of local solar radiation over the Tibetan Plateau compared to the temperature. Therefore, the remarkable HCHO daily variations are mainly connected with the variable weather over the Tibetan Plateau, which affects the natural emissions of HCHO precursors significantly.

Figure 11 shows the spatial distributions of the HCHO VCDs during the field campaign in July 2021. For the specific driving routes (XD, DY or YX), the HCHO spatial distributions were similar on different days. Normally, the HCHO VCDs were lager at the starting points and ending points of the driving routes (if reaching to the ending points in the condition of SZA < 80 °), which matched with the larger HCHO values in the morning and evening (Fig. 12). However, the HCHO levels were significantly different at the same location on different days. For example, the HCHO VCDs on the second circling journey (Fig. 11b1-b3) were obviously larger than those on the other three circling journeys, most probably due to higher surface temperatures on the second circling journey (Fig. ~~S4~~S7). From the northeast to the southwest in the region of the mobile observation field experiment, the HCHO VCDs present a decreasing trend. These lower HCHO levels in the main area of Three Rivers' Source reflect the overall conditions of atmospheric HCHO background. The spatial distributions of HCHO

column observed by the OMI satellite from 2009 to 2019 over the Tibetan Plateau also found that the regions with sparse population and less human activities were frequently affected by natural factors, such as air temperature and precipitation (Zhang et al., 2021). The elevated HCHO VCDs around Maqin county of the XD driving route were partly related to anthropogenic HCHO emissions, such as biomass burning and fossil fuel combustion (Fig. 11a1, b1, c1, d1) (Zhang et al., 2021). Comparing the HCHO VCDs before and after Maduo county on the YX driving route, the former was larger than the later, corresponding to the jump of the HCHO diurnal variation before and after 13:00 BJT (Fig. 12d). Besides the differences in human activities, the spatial step changes in the HCHO VCDs were also partly connected with the decreasing altitudes on the YX driving route (Fig. 2b).

With respect to the total means and medians of the HCHO VCDs in the range of 1.92–4.36 $\times 10^{15}$ molec $cm^{-2}$ (Fig. 12a), their diurnal variations are rather consistent during the whole day. They slightly decrease before 10:00 BJT and increase after 18:00 BJT, and also have no significant differences in the standard deviations. However, the diurnal variations of the HCHO VCDs are obviously different both for different days of the same driving route or among different driving routes (Fig. 12b-d). On average, the diurnal pattern of the HCHO VCDs during the XD driving route presents a weak "U" shape, i.e. slightly higher HCHO levels in the morning and evening. For the DY driving route, the total averaged HCHO VCDs almost maintain the level around 2 $\times 10^{15}$ molec $cm^{-2}$ before 14:00 BJT, and then gradually increase until the end of the DY journey. The diurnal pattern of the HCHO VCDs for the YX driving route presents a "W" shape, i.e. higher HCHO VCDs occur around 13:00 BJT, in the morning and in the evening. The variable diurnal cycles of HCHO VCDs were also found by ship-based MAX-DOAS measurements over the middle and lower Yangtze River in winter, where the both primary sources and photochemical secondary formation have large influences (Hong et al., 2018). Even at the starting and ending points of the driving route, there were almost no strong HCHO primary sources caused by anthropogenic activities over the Three Rivers' Source region. Thus we infer that the variable diurnal patterns of HCHO were mainly connected with the secondary photochemical formation of active VOCs emitted from vegetation (Mu et al., 2007). Meanwhile, due to the varying local microclimates over the Tibetan Plateau as well as different types and amounts of vegetation at different altitudes, the diurnal variations of secondary HCHO production are quite changeable and closely related to the specific property of a location. More comprehensive observations are needed over the Tibetan Plateau in the future to deeply understand the HCHO spatio-temporal evolution.

### 4.3 Comparison with TROPOMI observations

The TROPOspheric Monitoring Instrument (TROPOMI) is the sole payload on the Copernicus Sentinel-5 Precursor (Sentinel-5P or S5P) satellite, which provides measurements of multiple atmospheric trace species including $NO_2$ and HCHO at high spatial and temporal resolutions (Veefkind et al., 2012). The S5P reference orbit is a near-polar sun-synchronous orbit with a mean Local Solar Time of 13:30 at Ascending Node. TROPOMI covers the wavelength ranges of ultraviolet-visible (270~495 nm), near infrared (675~775 nm), and shortwave infrared (2305~2385 nm) with a 108° Field-of-View in nadir view. TROPOMI achieves daily global coverage with a spatial resolution of 5.5×3.5 $km^2$ at nadir since the along-track pixel size

reduction on August 6, 2019. The $NO_2$ retrieval consists of a three-step procedure: (1) The total $NO_2$ SCDs are retrieved from the Level-1b spectra measured by TROPOMI using the DOAS method; (2) The total $NO_2$ SCDs are separated into stratospheric SCDs and tropospheric SCDs on the basis of information coming from a data assimilation system; (3) The tropospheric $NO_2$ SCDs are converted into VCDs through a look-up table of tropospheric AMFs. The 1st and 3rd steps also apply to HCHO, but in addition, a bias of the HCHO SCDs needs to be corrected before the conversion of the HCHO SCDs to VCDs. In this study, we use the TROPOMI level-2 $NO_2$ and HCHO products (i.e. S5P_L2__NO2____HiR and S5P_L2__HCHO___HiR) downloaded from the NASA Goddard Earth Sciences Data and Information Services Center (GES-DISC) (ESA and KNMI, 2021; ESA and DLR, 2020). For comparison between the mobile MAX-DOAS and TROPOMI observations, their $NO_2$ and HCHO VCDs are gridded into 0.25 °×0.25 °cells (Fig. 13, 14). The reason for averaging two data sets into 0.25 °×0.25 °grid is to balance the spatial resolution and the amount of observed $NO_2$ and HCHO VCDs at specific grid cell. The TROPOMI relative precisions in the '$\Delta T_{1.5}$' situation (explained below) are estimated to be 72% and 113% for tropospheric $NO_2$ and HCHO VCDs, derived from the products of S5P_L2__NO2____HiR and S5P_L2__HCHO___HiR, respectively.

Figure 13 shows the spatial distributions of the tropospheric gridded $NO_2$ VCDs from TROPOMI on each day of the field campaign. The spatial distributions of the tropospheric $NO_2$ VCDs are basically consistent on different days, i.e. higher values are found in the northeast and lower values in the southwest. Similar as for the mobile MAX-DOAS, the TROPOMI $NO_2$ VCDs are larger around Xining city than in the main area of Three Rivers' Source region. But the elevated trends of the tropospheric $NO_2$ VCDs around the counties, which are clearly observed by the mobile MAX-DOAS, are nearly not captured by TROPOMI. To validate the fine-scale (0.25 °×0.25 °) spatial variability in tropospheric $NO_2$ VCDs, we made a linear regression analysis between both data sets (Fig. 15a). When using all tropospheric $NO_2$ VCDs at the same grid cell on the same day during the field campaign (referred to 'All' in Fig. 15a, corresponding to the white circles in Fig. 13), the consistency is good with a correlation coefficient of R=0.67 between the two data sets. However, the slope is much lower than unity indicating that the $NO_2$ VCDs from TROPOMI are systematically lower than those from mobile MAX-DOAS over the polluted areas. Besides of the probable underestimation of TROPOMI, the lower TROPOMI $NO_2$ VCDs are also connected with the time differences between the two observation methods at the same grid cell. In contrast~~Interestingly~~, there is almost no correlation of the two data sets, if we only use the tropospheric $NO_2$ VCDs within the 1.5 h time difference between mobile MAX-DOAS and TROPOMI at the same grid (referred to '$\Delta T_{1.5}$' in Fig. 15a, corresponding to the red pluses in Fig. 13). The weak correlation is to be understandable, because: (1) The level and the range variation of the $NO_2$ VCDs are very small in the background atmosphere over the Tibetan Plateau; (2) The signal-to-noise ratio is reduced due to the measurement errors for both MAX-DOAS and TROPOMI, introduced by the spectral analysis, ground slope, and the applied tropospheric AMF. Comparing the situations of 'All' and '$\Delta T_{1.5}$', significant differences in the correlation are connected with the former including the larger $NO_2$ VCDs close to the cities, inferred by the locations of the grid cell in Fig. 13. For the '$\Delta T_{1.5}$' comparison, mostly the low background values are included. These results indicate the TROPOMI can distinguish the differences in tropospheric $NO_2$ VCDs between city and background atmosphere over the Tibetan Plateau. Relative to the $NO_2$ VCDs by mobile MAX-DOAS during the field campaign, the relative (absolute) differences of the $NO_2$ VCDs by TROPOMI are -12% (-9.47 $\times 10^{13}$

molec cm$^{-2}$) and 40% (1.77 ×10$^{14}$ molec cm$^{-2}$) for 'All' and '$\Delta T_{1.5}$' on average, respectively. The positive bias for '$\Delta T_{1.5}$' is probably related to the horizontal $NO_2$ inhomogeneity, caused by mountain terrains over the main area of the Three Rivers' Source. However, without detailed knowledge about the true three-dimensional $NO_2$ distribution, this bias can not be fully understood in direction and magnitude. As a whole, in contrast to routine TROPOMI validation based on site observations (Verhoelst et al., 2021), the mobile MAX-DOAS observations can serve as a supplement to quantify the impact of the fine-scale $NO_2$ horizontal variability on satellite products.

In contrast to $NO_2$, the spatial distributions of the tropospheric gridded HCHO VCDs from TROPOMI are not uniform among different days of the field campaign (Fig. 14). The higher HCHO VCDs appear more in the second circling journey and the lower HCHO VCDs in the third and fourth circling journey, consistent with the aforementioned results derived from mobile MAX-DOAS. The HCHO levels around the city of Xining are also not significantly enhanced, even lower than those in the main area of the Three Rivers' Source region on some days, such as 25 July 2021. We also perform a linear regression analysis of tropospheric HCHO VCDs derived from mobile MAX-DOAS and TROPOMI, respectively. Whether for 'All' (corresponding to the white circles in Fig. 14) situation or for '$\Delta T_{1.5}$' (corresponding to the red pluses in Fig. 14) situation, the correlation coefficients are the same (R=0.26 in Fig. 15b), indicating that there are no strong anthropogenic HCHO sources along the driving routes even in the city of Xining. The rather small correlation coefficient between the two data sets is also related to the rather small variability of the HCHO VCDs and the relatively low signal-to-noise ratio of the TROPOMI satellite product in background atmosphere over the Tibetan Plateau. Comparing the '$\Delta T_{1.5}$' situation between $NO_2$ and HCHO, the correlation of the tropospheric HCHO VCDs is higher than that of $NO_2$, which is probably related to the stronger HCHO daily variations in the background atmosphere influenced by natural factors, such as air temperature and precipitation (Zhang et al., 2021). Similar to the validations of TROPOMI at remote sites by ground-based solar-absorption Fourier-transform infrared (FTIR) measurements (Vigouroux et al., 2020), an overestimation of the true HCHO VCD by TROPOMI is also found during the field campaign, with significantly larger relative (absolute) differences of 104% (2.60 ×10$^{15}$ molec cm$^{-2}$) and 87% (2.16 ×10$^{15}$ molec cm$^{-2}$) for 'All' and '$\Delta T_{1.5}$' on average, respectively (Fig. 15b). This large positive offset of the TROPOMI HCHO VCDs is probably connected with the horizontal HCHO inhomogeneity, caused by mountain terrain and varying local microclimates over the Tibetan Plateau. Therefore, although TROPOMI significantly improves the precision of the HCHO observations at short temporal scales and for low HCHO columns (De Smedt et al., 2021), it is still a challenge for satellite instruments to detect the spatio-temporal variations of HCHO over the Tibetan Plateau.

## 5 Summary and conclusions

In this study we performed mobile MAX-DOAS measurements over the Tibetan Plateau in summer (18–30 July) 2021 for the first time. We analysed spectra of scattered sun light collected in the Three Rivers' Source region over the Tibetan Plateau, and obtained the data sets of tropospheric $NO_2$ and HCHO VCDs in the background atmosphere; We further investigated the

abundances and spatio-temporal variations of the tropospheric $NO_2$ and HCHO VCDs, and validated the TROPOMI satellite products during the field campaign.

We tested the influences of different Fraunhofer reference spectra (FRSs) and different spectral intervals on the spectral retrieval, and found that the fitting residuals are smaller when using the sequential FRSs in the $NO_2$ visible wavelength region for mobile MAX-DOAS measurements in the background atmosphere over mountain terrain. After investigating the optimal filters to eliminate the "bad measurements" caused by sunlight shelters and vehicle's vibration and bumpiness, the $NO_2$ and HCHO DSCDs were retained with the conditions of (1) RMS < 0.005, (2) offset (constant) between ± 0.03, and (3) SZA < 80 °. The qualified $NO_2$ and HCHO DSCDs were converted to the corresponding VCDs based on the air mass factor (AMF) estimated by the geometric approximation method. Through comparing the resulting $NO_2$ and HCHO VCDs at three different elevation angles (15°, 20°, 30°), the $VCD_{15°}$ were further filtered and kept as the final data sets of tropospheric $NO_2$ and HCHO VCDs when absolute and relative VCD differences (ΔVCD) between 15 °and 20 °are < $10^{15}$ molec $cm^{-2}$ or <5% for $NO_2$ and < $2\times10^{15}$ molec $cm^{-2}$ or <5% for HCHO, respectively.

The background levels ± standard deviations of tropospheric $NO_2$ and HCHO VCDs, estimated by the maximum frequency method, were 0.40 ± 1.13~~0.23~~ × $10^{15}$ molec $cm^{-2}$ for $NO_2$ and 2.27 ± 1.66~~0.96~~ ×$10^{15}$ molec $cm^{-2}$ for HCHO in July 2021 over the Three Rivers' Source region. We also determined the dependence of the tropospheric $NO_2$ and HCHO VCDs on altitude, which generally presents a decreasing trend with the increasing altitude. This characteristic for natural background atmosphere is probably mainly related to the lower air density at higher altitude. However, different from the nearly constant decreasing rate of HCHO VCDs with increasing altitude, the differences of decreasing rate above and below the 2750 m altitude for $NO_2$ VCDs are significant, which is highly connected with different contributions of anthropogenic sources and natural sources for $NO_2$ and HCHO.

With respect to the spatio-temporal distributions, the day-to-day variations of the $NO_2$ VCDs between different circling journeys were similar, i.e. similar geographical distributions of the $NO_2$ VCDs were observed for each circling journey. The tropospheric $NO_2$ VCDs over the main area of Three Rivers' Source were relatively uniform with very low levels (<$1\times10^{15}$ molec $cm^{-2}$), but they were usually elevated in cities or counties, around the Qinghai Lake, even occasionally at the highway junction and the tunnel exit, where there were enhanced transport emissions. The daytime diurnal patterns of $NO_2$ VCDs, i.e. higher values in the morning and evening, could also reflect the differences of the $NO_2$ spatial distribution. Based on radiative transfer simulations we can rule out that the stratospheric $NO_2$ absorption can explain the observed diurnal cycle of the tropospheric $NO_2$ VCD. Besides the enhanced $NO_2$ photolysis around noon, the enhanced $NO_2$ VCDs in the morning and evening were primarily caused by enhanced pollution levels when the mobile observation vehicle was located in or close to the cities or county towns. However, the day-to-day variations of the HCHO VCDs were highly correlated to the air temperature and significantly different between different circling journeys. Overall, the HCHO VCDs presented a decreasing trend from the northeast to the southwest in the region of the field experiment. The HCHO VCDs were elevated at the starting points and ending points of the driving routes, corresponding to larger HCHO VCDs in the morning and evening. The levels

of the HCHO VCDs were variable on different days at the same location, implying that natural factors, such as air temperature, significantly influenced the atmospheric HCHO photochemical formation.

TROPOMI $NO_2$ clearly presents the obvious influences of anthropogenic sources on enhanced $NO_2$ VCDs around Xining city, i.e. it can distinguish the differences in tropospheric $NO_2$ VCDs between the city and the background atmosphere over the region of the field campaign. But the elevated trends of the tropospheric $NO_2$ VCDs around the counties over the main area of the Three Rivers' Source region, which are clearly observed by the mobile MAX-DOAS, are nearly not captured by TROPOMI. In contrast, the stronger influences of natural factors on HCHO lead to larger daily variation of HCHO, which causes inconsistent and variable spatial distributions of TROPOMI HCHO VCDs on different days but also a higher correlation between mobile MAX-DOAS and TROPOMI than $NO_2$ for the background atmosphere. The positive offsets of TROPOMI $NO_2$ and HCHO VCDs are 40% and 87% on average, respectively. This is probably caused by mountain terrains and varying local microclimates over the main area of the Three Rivers' Source region.

As a whole, we obtained valuable data sets and information of the spatio-temporal variation of $NO_2$ and HCHO over the Tibetan Plateau, which have the great potential in investigating the evolution of the atmospheric composition in the background atmosphere at high altitude, validating and improving the satellite products over mountain terrain, and evaluating atmospheric chemistry model over the Tibetan Plateau.

**Code and data availability.** The filtered final $NO_2$ and HCHO VCDs for the field campaign by mobile MAX-DOAS observations on 18-30 July 2021 over the Three Rivers' Source region of the Tibetan Plateau in China are available upon request.

**Supplement.** The supplement related to this article is available online.

**Author contributions.** X.H. Cheng and X.D. Xu designed the field experiment. S.Y. Cheng and J.Z. Ma set up the mobile MAX-DOAS measurement platform under discussions with X.H. Cheng, J.G. Lv, S. Dörner, S. Donner, and T. Wagner. W.Q. Zhang, G. Bai, B. Chen, and S.Y. Ma contributed to the field measurements. S.Y. Cheng performed the spectra retrieval and data analysis with contributions from T. Wagner, S. Dörner, S. Donner, and J.Z. Ma. S.Y. Cheng, J.Z. Ma, and T. Wagner prepared the manuscript with consent by all co-authors.

**Competing interests.** The authors declare that they have no conflict of interest.

**Acknowledgements.** We thank the staff at the Qinghai Meteorological Administration for supporting the measurements. We thank BIRA-IASB for QDOAS spectral analysis software. We also thank ESA, KNMI, DLR and NASA for the TROPOMI satellite products.

**Financial support.** This research is supported by grants from the Fundamental Research Funds for Central Public-interest Scientific Institution from Chinese Academy of Meteorological Sciences (No. 2021Z013), the National Natural Science Foundation of China (No. 41875146), and the Fund of State Key Laboratory of Applied Optics (No. SKLAO2021001A02).

**References**


Bolin, B.: On the Influence of the Earth's Orography on the General Character of the Westerlies, Tellus, 2, 184-195, 10.3402/tellusa.v2i3.8547, 1950.

Boos, W. R. and Kuang, Z.: Dominant control of the South Asian monsoon by orographic insulation versus plateau heating, Nature, 463, 218-222, 10.1038/nature08707, 2010.

Borovski, A. N., Dzhola, A. V., Elokhov, A. S., Grechko, E. I., Kanaya, Y., and Postylyakov, O. V.: First measurements of formaldehyde integral content in the atmosphere using MAX-DOAS in the Moscow Region, International Journal of Remote Sensing, 35, 5609-5627, 10.1080/01431161.2014.945011, 2014.

Brinksma, E. J., Pinardi, G., Volten, H., Braak, R., Richter, A., Schönhardt, A., van Roozendael, M., Fayt, C., Hermans, C., Dirksen, R. J., Vlemmix, T., Berkhout, A. J. C., Swart, D. P. J., Oetjen, H., Wittrock, F., Wagner, T., Ibrahim, O. W., de Leeuw, G., Moerman, M., Curier, R. L., Celarier, E. A., Cede, A., Knap, W. H., Veefkind, J. P., Eskes, H. J., Allaart, M., Rothe, R., Piters, A. J. M., and Levelt, P. F.: The 2005 and 2006 DANDELIONS $NO_2$ and aerosol intercomparison campaigns, Journal of Geophysical Research, 113, D16S46, 10.1029/2007jd008808, 2008.

Chen, P., Kang, S., Yang, J., Pu, T., Li, C., Guo, J., and Tripathee, L.: Spatial and Temporal Variations of Gaseous and Particulate Pollutants in Six Sites in Tibet, China, during 2016–2017, Aerosol and Air Quality Research, 19, 516-527, 10.4209/aaqr.2018.10.0360, 2019.

Cheng, S., Wang, Y., and An, X.: Temporal Variation and Source Identification of Black Carbon at Lin'an and Longfengshan Regional Background Stations in China, Journal of Meteorological Research, 31, 1070-1084, 10.1007/s13351-017-7030-5, 2017.

Cheng, S., Jin, J., Ma, J., Lv, J., Liu, S., and Xu, X.: Temporal Variation of $NO_2$ and HCHO Vertical Profiles Derived from MAX-DOAS Observation in Summer at a Rural Site of the North China Plain and Ozone Production in Relation to HCHO/$NO_2$ Ratio, Atmosphere, 13, 860, 10.3390/atmos13060860, 2022.

Cheng, S., Ma, J., Cheng, W., Yan, P., Zhou, H., Zhou, L., and Yang, P.: Tropospheric $NO_2$ vertical column densities retrieved from ground-based MAX-DOAS measurements at Shangdianzi regional atmospheric background station in China, J Environ Sci (China), 80, 186-196, 10.1016/j.jes.2018.12.012, 2019.

Cheng, S., Ma, J., Zheng, X., Gu, M., Donner, S., Dörner, S., Zhang, W., Du, J., Li, X., Liang, Z., Lv, J., and Wagner, T.: Retrieval of $O_3$, $NO_2$, BrO and OClO Columns from Ground-Based Zenith Scattered Light DOAS Measurements in Summer and Autumn over the Northern Tibetan Plateau, Remote Sensing, 13, 4242, 10.3390/rs13214242, 2021.

Coburn, S., Dix, B., Sinreich, R., and Volkamer, R.: The CU ground MAX-DOAS instrument: characterization of RMS noise limitations and first measurements near Pensacola, FL of BrO, IO, and CHOCHO, Atmospheric Measurement Techniques, 4, 2421-2439, 10.5194/amt-4-2421-2011, 2011.

Danckaert, T., Fayt, C., Roozendael, M. V., Smedt, I. D., Letocart, V., Merlaud, A., and Pinardi, G.: QDOAS Software user manual, Belgian Institute for Space Aeronomy, Brussels, Belgium, 2017.

De Smedt, I., Pinardi, G., Vigouroux, C., Compernolle, S., Bais, A., Benavent, N., Boersma, F., Chan, K.-L., Donner, S., Eichmann, K.-U., Hedelt, P., Hendrick, F., Irie, H., Kumar, V., Lambert, J.-C., Langerock, B., Lerot, C., Liu, C., Loyola, D., Piters, A., Richter, A., Rivera Cárdenas, C., Romahn, F., Ryan, R. G., Sinha, V., Theys, N., Vlietinck, J., Wagner, T., Wang, T., Yu, H., and Van Roozendael, M.: Comparative assessment of TROPOMI and OMI formaldehyde observations and validation against MAX-DOAS network column measurements, Atmospheric Chemistry and Physics, 21, 12561-12593, 10.5194/acp-21-12561-2021, 2021.

Deutschmann, T., Beirle, S., Frieß, U., Grzegorski, M., Kern, C., Kritten, L., Platt, U., Prados-Román, C., Puķīte, J., Wagner, T., Werner, B., and Pfeilsticker, K.: The Monte Carlo atmospheric radiative transfer model McArtim: Introduction and validation of Jacobians and 3D features, Journal of Quantitative Spectroscopy and Radiative Transfer, 112, 1119-1137, 10.1016/j.jqsrt.2010.12.009, 2011.

Dong, W., Lin, Y., Wright, J. S., Xie, Y., Xu, F., Xu, W., and Wang, Y.: Indian Monsoon Low-Pressure Systems Feed Up-and-Over Moisture Transport to the Southwestern Tibetan Plateau, Journal of Geophysical Research: Atmospheres, 122, 12,140-112,151, 10.1002/2017jd027296, 2017.

Donner, S.: Mobile MAX-DOAS measurements of the tropospheric formaldehyde column in the Rhein-Main region, Master thesis, University of Mainz, Mainz, 2016.

Duan, A., Zhang, Q., Liu, Y., Wu, G., Wang, T., Wan, R., Liu, X., Li, W., Wang, Z., and Liang, X.: The Influence of Mechanical and Thermal Forcing by the Tibetan Plateau on Asian Climate, Journal of Hydrometeorology, 8, 770-789, 10.1175/jhm609.1, 2007.

Duo, B., Cui, L., Wang, Z., Li, R., Zhang, L., Fu, H., Chen, J., Zhang, H., and Qiong, A.: Observations of atmospheric pollutants at Lhasa during 2014-2015: Pollution status and the influence of meteorological factors, J Environ Sci (China), 63, 28-42, 10.1016/j.jes.2017.03.010, 2018.

ESA and DLR: Sentinel-5P TROPOMI Tropospheric Formaldehyde HCHO 1-Orbit L2 5.5km x 3.5km, Goddard Earth Sciences Data and Information Services Center (GES DISC) [dataset], 10.5270/S5P-vg1i7t0, 2020.

ESA and KNMI: Sentinel-5P TROPOMI Tropospheric $NO_2$ 1-Orbit L2 5.5km x 3.5km, Goddard Earth Sciences Data and Information Services Center (GES DISC) [dataset], 10.5270/S5P-9bnp8q8, 2021.

Franco, B., Hendrick, F., Van Roozendael, M., Müller, J. F., Stavrakou, T., Marais, E. A., Bovy, B., Bader, W., Fayt, C., Hermans, C., Lejeune, B., Pinardi, G., Servais, C., and Mahieu, E.: Retrievals of formaldehyde from ground-based FTIR and MAX-DOAS observations at the Jungfraujoch station and comparisons with GEOS-Chem and IMAGES model simulations, Atmospheric Measurement Techniques, 8, 1733-1756, 10.5194/amt-8-1733-2015, 2015.

Gao, J., Yao, T., Masson-Delmotte, V., Steen-Larsen, H. C., and Wang, W.: Collapsing glaciers threaten Asia's water supplies, Nature, 565, 19-21, 10.1038/d41586-018-07838-4, 2019.

Gil-Ojeda, M., Navarro-Comas, M., Gómez-Martín, L., Adame, J. A., Saiz-Lopez, A., Cuevas, C. A., González, Y., Puentedura, O., Cuevas, E., Lamarque, J. F., Kinninson, D., and Tilmes, S.: $NO_2$ seasonal evolution in the north subtropical free troposphere, Atmospheric Chemistry and Physics, 15, 10567-10579, 10.5194/acp-15-10567-2015, 2015.

Gomez, L., Navarro-Comas, M., Puentedura, O., Gonzalez, Y., Cuevas, E., and Gil-Ojeda, M.: Long-path averaged mixing ratios of $O_3$ and $NO_2$ in the free troposphere from mountain MAX-DOAS, Atmospheric Measurement Techniques, 7, 3373-3386, 10.5194/amt-7-3373-2014, 2014.

Granier, C., Bessagnet, B., Bond, T., D'Angiola, A., Denier van der Gon, H., Frost, G. J., Heil, A., Kaiser, J. W., Kinne, S., Klimont, Z., Kloster, S., Lamarque, J.-F., Liousse, C., Masui, T., Meleux, F., Mieville, A., Ohara, T., Raut, J.-C., Riahi, K., Schultz, M. G., Smith, S. J., Thompson, A., van Aardenne, J., van der Werf, G. R., and van Vuuren, D. P.: Evolution of anthropogenic and biomass burning emissions of air pollutants at global and regional scales during the 1980–2010 period, Climatic Change, 109, 163-190, 10.1007/s10584-011-0154-1, 2011.

Guo, F., Bao, M., Mu, Y., Liu, Z., Li, Y., and Shi, H.: Temporal and spatial characteristics of lightning-produced nitrogen oxides in China, Journal of Atmospheric and Solar-Terrestrial Physics, 149, 100-107, 10.1016/j.jastp.2016.10.007, 2016.

He, J., Gong, S., Yu, Y., Yu, L., Wu, L., Mao, H., Song, C., Zhao, S., Liu, H., Li, X., and Li, R.: Air pollution characteristics and their relation to meteorological conditions during 2014–2015 in major Chinese cities, Environmental Pollution, 223, 484-496, 10.1016/j.envpol.2017.01.050, 2017.

Hong, Q., Liu, C., Chan, K. L., Hu, Q., Xie, Z., Liu, H., Si, F., and Liu, J.: Ship-based MAX-DOAS measurements of tropospheric $NO_2$, $SO_2$, and HCHO distribution along the Yangtze River, Atmospheric Chemistry and Physics, 18, 5931-5951, 10.5194/acp-18-5931-2018, 2018.

Hönninger, G., Friedeburg, C. v., and Platt, U.: Multi axis differential optical absorption spectroscopy (MAX-DOAS), Atmospheric Chemistry and Physics, 4, 231-254, 10.5194/acp-4-231-2004, 2004.

Kang, S., Zhang, Q., Zhang, Y., Guo, W., Ji, Z., Shen, M., Wang, S., Wang, X., Tripathee, L., Liu, Y., Gao, T., Xu, G., Gao, Y., Kaspari, S., Luo, X., and Mayewski, P.: Warming and thawing in the Mt. Everest region: A review of climate and environmental changes, Earth-Science Reviews, 225, 103911, 10.1016/j.earscirev.2021.103911, 2022.

Kurokawa, J., Ohara, T., Morikawa, T., Hanayama, S., Janssens-Maenhout, G., Fukui, T., Kawashima, K., and Akimoto, H.: Emissions of air pollutants and greenhouse gases over Asian regions during 2000–2008: Regional Emission inventory in ASia (REAS) version 2, Atmospheric Chemistry and Physics, 13, 11019-11058, 10.5194/acp-13-11019-2013, 2013.

Lee, D. S., Köhler, I., Grobler, E., Rohrer, F., Sausen, R., Gallardo-Klenner, L., Olivier, J. G. J., Dentener, F. J., and Bouwman, A. F.: Estimations of global $NO_x$ emissions and their uncertainties, Atmospheric Environment, 31, 1735-1749, 10.1016/s1352-2310(96)00327-5, 1997.

Liu, Y., Hoskins, B., and Blackburn, M.: Impact of Tibetan Orography and Heating on the Summer Flow over Asia, Journal of the Meteorological Society of Japan. Ser. II, 85B, 1-19, 10.2151/jmsj.85B.1, 2007.

Ma, J., Zhou, X., Xu, X., Xu, X., Gromov, S., and Lelieveld, J.: Ozone and aerosols over the Tibetan Plateau, in: Asian Atmospheric Pollution: Sources, Characteristics and Impacts, edited by: Singh, R. P., Elsevier, Amsterdam, Netherlands, 287-302, 2021.

Ma, J., Brühl, C., He, Q., Steil, B., Karydis, V. A., Klingmüller, K., Tost, H., Chen, B., Jin, Y., Liu, N., Xu, X., Yan, P., Zhou, X., Abdelrahman, K., Pozzer, A., and Lelieveld, J.: Modeling the aerosol chemical composition of the tropopause over the Tibetan Plateau during the Asian summer monsoon, Atmospheric Chemistry and Physics, 19, 11587-11612, 10.5194/acp-19-11587-2019, 2019.

Ma, J., Dörner, S., Donner, S., Jin, J., Cheng, S., Guo, J., Zhang, Z., Wang, J., Liu, P., Zhang, G., Pukite, J., Lampel, J., and Wagner, T.: MAX-DOAS measurements of $NO_2$, $SO_2$, HCHO, and BrO at the Mt. Waliguan WMO GAW global baseline station in the Tibetan Plateau, Atmospheric Chemistry and Physics, 20, 6973-6990, 10.5194/acp-20-6973-2020, 2020.

Ma, J. Z., Tang, J., Zhou, X. J., and Zhang, X. S.: Estimates of the chemical budget for ozone at Waliguan Observatory, Journal of Atmospheric Chemistry, 41, 21-48, Doi 10.1023/A:1013892308983, 2002.

Ma, J. Z., Beirle, S., Jin, J. L., Shaiganfar, R., Yan, P., and Wagner, T.: Tropospheric $NO_2$ vertical column densities over Beijing: results of the first three years of ground-based MAX-DOAS measurements (2008-2011) and satellite validation, Atmospheric Chemistry and Physics, 13, 1547-1567, 10.5194/acp-13-1547-2013, 2013.

Marais, E. A., Roberts, J. F., Ryan, R. G., Eskes, H., Boersma, K. F., Choi, S., Joiner, J., Abuhassan, N., Redondas, A., Grutter, M., Cede, A., Gomez, L., and Navarro-Comas, M.: New observations of $NO_2$ in the upper troposphere from TROPOMI, Atmospheric Measurement Techniques, 14, 2389-2408, 10.5194/amt-14-2389-2021, 2021.

Mazière, M. D., Thompson, A. M., Kurylo, M. J., Wild, J. D., Bernhard, G., Blumenstock, T., Braathen, G. O., Hannigan, J. W., Lambert, J.-C., Leblanc, T., McGee, T. J., Nedoluha, G., Petropavlovskikh, I., Seckmeyer, G., Simon, P. C., Steinbrecht, W., and Strahan, S. E.: The Network for the Detection of Atmospheric Composition Change (NDACC): history, status and perspectives, Atmos. Chem. Phys., 18, 4935–4964, 10.5194/acp-18-4935-2018, 2018.

Meng, Z.-Y., Xu, X.-B., Wang, T., Zhang, X.-Y., Yu, X.-L., Wang, S.-F., Lin, W.-L., Chen, Y.-Z., Jiang, Y.-A., and An, X.-Q.: Ambient sulfur dioxide, nitrogen dioxide, and ammonia at ten background and rural sites in China during 2007–2008, Atmospheric Environment, 44, 2625-2631, 10.1016/j.atmosenv.2010.04.008, 2010.

Mu, Y., Pang, X., Quan, J., and Zhang, X.: Atmospheric carbonyl compounds in Chinese background area: A remote mountain of the Qinghai-Tibetan Plateau, Journal of Geophysical Research, 112, 10.1029/2006jd008211, 2007.

Platt, U. and Stutz, J.: Differential Optical absorption spectroscopy, Principles and Applications, Springer, Berlin, 2008.

Qiu, J.: China: The third pole, Nature, 454, 393-396, 10.1038/454393a, 2008.

Ran, L., Lin, W. L., Deji, Y. Z., La, B., Tsering, P. M., Xu, X. B., and Wang, W.: Surface gas pollutants in Lhasa, a highland city of Tibet-current levels and pollution implications, Atmospheric Chemistry and Physics, 14, 10721-10730, 10.5194/acp-14-10721-2014, 2014.

Schreier, S. F., Richter, A., Wittrock, F., and Burrows, J. P.: Estimates of free-tropospheric $NO_2$ and HCHO mixing ratios derived from high-altitude mountain MAX-DOAS observations at midlatitudes and in the tropics, Atmospheric Chemistry and Physics, 16, 2803-2817, 10.5194/acp-16-2803-2016, 2016.

Seinfeld, J. H. and Pandis, S. N.: Atmospheric Chemistry and Physics: From Air Pollution to Climate Change, 3rd Edn., John Wiley & Sons, Inc., Hoboken, New Jersey, USA, 2016.

Singh, R. P.: Asian Atmospheric Pollution: Sources, Characteristics and Impacts, Elsevier, Amsterdam, Netherlands, 2021.

Stavrakou, T., Müller, J. F., De Smedt, I., Van Roozendael, M., van der Werf, G. R., Giglio, L., and Guenther, A.: Evaluating the performance of pyrogenic and biogenic emission inventories against one decade of space-based formaldehyde columns, Atmospheric Chemistry and Physics, 9, 1037-1060, 10.5194/acp-9-1037-2009, 2009.

Stutz, J. and Platt, U.: Numerical analysis and estimation of the statistical error of differential optical absorption spectroscopy measurements with least-squares methods, Appl. Opt., 35, 6041-6053, 10.1364/AO.35.006041, 1996.

Veefkind, J. P., Aben, I., McMullan, K., Förster, H., Vries, J. d., Otter, G., Claas, J., Eskes, H. J., Haan, J. F. d., Kleipool, Q., Weele, M. v., Hasekamp, O., Hoogeveen, R., Landgraf, J., Snel, R., Tol, P., Ingmann, P., Voors, R., Kruizinga, B., Vink, R., Visser, H., and Levelt, P. F.: TROPOMI on the ESA Sentinel-5 Precursor: A GMES mission for global observations of the atmospheric composition for climate, air quality and ozone layer applications, Remote Sensing of Environment, 120, 70-83, 10.1016/j.rse.2011.09.027, 2012.

Verhoelst, T., Compernolle, S., Pinardi, G., Lambert, J.-C., Eskes, H. J., Eichmann, K.-U., Fjæraa, A. M., Granville, J., Niemeijer, S., Cede, A., Tiefengraber, M., Hendrick, F., Pazmiño, A., Bais, A., Bazureau, A., Boersma, K. F., Bognar, K., Dehn, A., Donner, S., Elokhov, A., Gebetsberger, M., Goutail, F., Grutter de la Mora, M., Gruzdev, A., Gratsea, M., Hansen, G. H., Irie, H., Jepsen, N., Kanaya, Y., Karagkiozidis, D., Kivi, R., Kreher, K., Levelt, P. F., Liu, C., Müller, M., Navarro Comas, M., Piters, A. J. M., Pommereau, J.-P., Portafaix, T., Prados-Roman, C., Puentedura, O., Querel, R., Remmers, J., Richter, A., Rimmer, J., Rivera Cárdenas, C., Saavedra de Miguel, L., Sinyakov, V. P., Stremme, W., Strong, K., Van Roozendael, M., Veefkind, J. P., Wagner, T., Wittrock, F., Yela González, M., and Zehner, C.: Ground-based validation of the Copernicus Sentinel-5P TROPOMI $NO_2$ measurements with the NDACC ZSL-DOAS, MAX-DOAS and Pandonia global networks, Atmospheric Measurement Techniques, 14, 481-510, 10.5194/amt-14-481-2021, 2021.

Vigouroux, C., Langerock, B., Aquino, C. A. B., Blumenstock, T., Cheng, Z., Mazière, M. D., Smedt, I. D., Grutter, M., Hannigan, J. W., Jones, N., Kivi, R., Loyola, D., Lutsch, E., Mahieu, E., Makarova, M., Metzger, J.-M., Morino, I., Murata, I., Nagahama, T., Notholt, J., Ortega, I., Palm, M., Pinardi, G., Röhling, A., Smale, D., Stremme, W., Strong, K., Sussmann, R., Té, Y., Roozendael, M. v., Wang, P., and Winkler, H.: TROPOMI–Sentinel-5 Precursor formaldehyde validation using an extensive network of ground-based Fourier-transform infrared stations, Atmos. Meas. Tech., 13, 3751–3767, 10.5194/amt-13-3751-2020, 2020.

Wang, Q. Y., Gao, R. S., Cao, J. J., Schwarz, J. P., Fahey, D. W., Shen, Z. X., Hu, T. F., Wang, P., Xu, X. B., and Huang, R. J.: Observations of high level of ozone at Qinghai Lake basin in the northeastern Qinghai-Tibetan Plateau, western China, Journal of Atmospheric Chemistry, 72, 19-26, 10.1007/s10874-015-9301-9, 2015.

Wang, T., Wong, H. L. A., Tang, J., Ding, A., Wu, W. S., and Zhang, X. C.: On the origin of surface ozone and reactive nitrogen observed at a remote mountain site in the northeastern Qinghai-Tibetan Plateau, western China, Journal of Geophysical Research, 111, 10.1029/2005jd006527, 2006.

Wang, Y., Puķīte, J., Wagner, T., Donner, S., Beirle, S., Hilboll, A., Vrekoussis, M., Richter, A., Apituley, A., Piters, A., Allaart, M., Eskes, H., Frumau, A., Van Roozendael, M., Lampel, J., Platt, U., Schmitt, S., Swart, D., and Vonk, J.: Vertical Profiles of Tropospheric Ozone From MAX-DOAS Measurements During the CINDI-2 Campaign: Part 1-Development of a New Retrieval Algorithm, Journal of Geophysical Research: Atmospheres, 123, 10637-10670, 10.1029/2018jd028647, 2018.

Xing, C., Liu, C., Wu, H., Lin, J., Wang, F., Wang, S., and Gao, M.: Ground-based vertical profile observations of atmospheric composition on the Tibetan Plateau (2017–2019), Earth System Science Data, 13, 4897-4912, 10.5194/essd-13-4897-2021, 2021.

Xu, X., Lu, C., Shi, X., and Gao, S.: World water tower: An atmospheric perspective, Geophysical Research Letters, 35, 10.1029/2008gl035867, 2008.

Xu, X., Lin, W., Xu, W., Jin, J., Wang, Y., Zhang, G., Zhang, X., Ma, Z., Dong, Y., Ma, Q., Yu, D., Li, Z., Wang, D., and Zhao, H.: Long-term changes of regional ozone in China: implications for human health and ecosystem impacts, Elementa: Science of the Anthropocene, 8, Art. 13, 10.1525/elementa.409, 2020.

Xue, L. K., Wang, T., Guo, H., Blake, D. R., Tang, J., Zhang, X. C., Saunders, S. M., and Wang, W. X.: Sources and photochemistry of volatile organic compounds in the remote atmosphere of western China: results from the Mt. Waliguan Observatory, Atmospheric Chemistry and Physics, 13, 8551-8567, 10.5194/acp-13-8551-2013, 2013.

Xue, L. K., Wang, T., Zhang, J. M., Zhang, X. C., Deliger, Poon, C. N., Ding, A. J., Zhou, X. H., Wu, W. S., Tang, J., Zhang, Q. Z., and Wang, W. X.: Source of surface ozone and reactive nitrogen speciation at Mount Waliguan in western China: New insights from the 2006 summer study, Journal of Geophysical Research, 116, 10.1029/2010jd014735, 2011.

Yanai, M., Li, C., and Song, Z.: Seasonal Heating of the Tibetan Plateau and Its Effects on the Evolution of the Asian Summer Monsoon, Journal of the Meteorological Society of Japan. Ser. II, 70, 319-351, 10.2151/jmsj1965.70.1B_319, 1992.

Yang, J., Ji, Z., Kang, S., Zhang, Q., Chen, X., and Lee, S.-Y.: Spatiotemporal variations of air pollutants in western China and their relationship to meteorological factors and emission sources, Environmental Pollution, 254, 112952, 10.1016/j.envpol.2019.07.120, 2019.

Zhang, Y., Ju, T., Shi, Y., Wang, Q., Li, F., and Zhang, G.: Analysis of spatiotemporal variation of formaldehyde column concentration in Qinghai-Tibet Plateau and its influencing factors, Environ Sci Pollut Res Int, 28, 55233-55251, 10.1007/s11356-021-14719-3, 2021.

Zhao, R., Dou, X., Zhang, N., Zhao, X., Yang, W., Han, B., Yu, H., Azzi, M., Wang, Y., and Bai, Z.: The characteristics of inorganic gases and volatile organic compounds at a remote site in the Tibetan Plateau, Atmospheric Research, 234, 104740, 10.1016/j.atmosres.2019.104740, 2020.

Zhou, X., Zhao, P., Chen, J., Chen, L., and Li, W.: Impacts of thermodynamic processes over the Tibetan Plateau on the Northern Hemispheric climate, Science in China Series D: Earth Sciences, 52, 1679-1693, 10.1007/s11430-009-0194-9, 2009.

**Table 1.** Observation periods and routes of the mobile MAX-DOAS field experiment over the Three Rivers' Source region of the Tibetan Plateau in July 2021.

| Cycles | Xining to Dari (XD) | Dari to Yushu (DY) | Yushu to Xining (YX) |
|---|---|---|---|
| 1 | 2021-07-18 9:00~22:49BJT[a] | 2021-07-19 9:05~17:40BJT | 2021-07-20 8:17~21:48BJT |
| 2 | 2021-07-21 8:09~21:40BJT | 2021-07-22 8:20~16:07BJT | 2021-07-23 8:18~21:38BJT |
| 3 | 2021-07-25 8:29~20:08BJT | 2021-07-26 8:08~15:20BJT | 2021-07-27 8:18~21:48BJT |
| 4 | 2021-07-28 8:27~18:56BJT | 2021-07-29 9:00~16:00BJT | 2021-07-30 8:21~22:35BJT |

[a] BJT denotes the Beijing time, corresponding to Universal Time Coordinated (UTC) + 8 h.

780

**Table 2.** Fit settings for the $NO_2$ and HCHO spectral analyses.

| Parameters | Setting for $NO_2$ | Setting for HCHO |
|---|---|---|
| Fraunhofer reference spectrum | sequential spectra | sequential spectra |
| fitting interval (nm) | 400~434 | 324~359 |
| DOAS polynomial | degree: 5 | |
| intensity offset | degree: 2 (constant and order 1) | |
| shift and stretch | spectrum | |
| Ring spectra | original and wavelength-dependent Ring spectra | |
| $NO_2$ cross section | Vandaele et al. (1998), 294 K, $I_o$ correction ($10^{17}$ molec•cm$^{-2}$) | |
| $H_2O$ cross section | Polyansky et al. (2018), 293 K | / |
| $O_3$ cross section | Serdyuchenko et al. (2014), 223 K, $I_o$ correction ($10^{20}$ molec•cm$^{-2}$) | Serdyuchenko et al. (2014), 223 K, 243 K, $I_o$ correction ($10^{20}$ molec•cm$^{-2}$) |
| $O_4$ cross section | Thalman and Volkamer (2013), 293 K | Thalman and Volkamer (2013), 293 K |
| HCHO cross section | / | Meller and Moortgat (2000), 298 K |

**Table 3.** Statistics for the $NO_2$ and HCHO VCDs at the three elevation angles ($15^\circ$, $20^\circ$, $30^\circ$).

| Parameters | Mean (Median) ± Standard deviation ($10^{15}$ molec cm$^{-2}$) | | | Correlation Coefficient | | |
|---|---|---|---|---|---|---|
| | 15 ° | 20 ° | 30 ° | 15 °vs. 20 ° | 15 °vs. 30 ° | 20 °vs. 30 ° |
| $NO_2$ | 1.40 (0.57) ±2.61 | 1.42 (0.63) ±2.52 | 1.59 (0.82) ±2.70 | 0.95 | 0.91 | 0.94 |
| HCHO | 2.53 (2.35) ±1.97 | 2.81 (2.69) ±2.60 | 3.25 (3.20) ±4.09 | 0.80 | 0.66 | 0.73 |

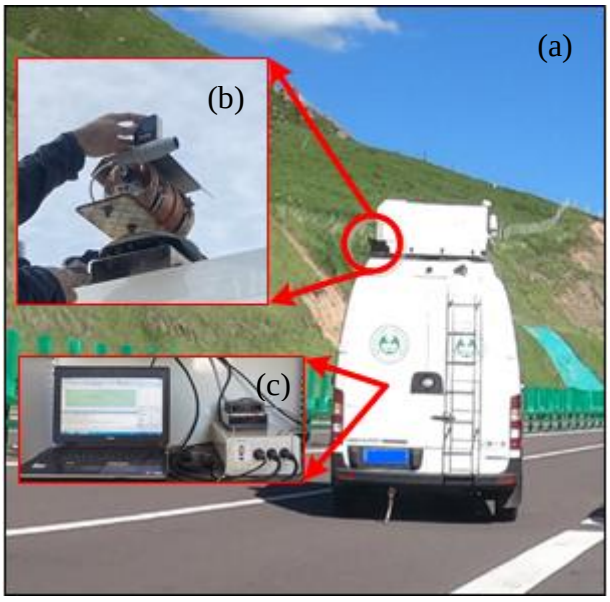


**Figure 1. (a)** Mobile observation vehicle of atmospheric composition and meteorological parameters. Two parts of the Tube MAX-DOAS instrument are installed **(b)** on the rear of the vehicle's roof and **(c)** inside the vehicle, respectively.

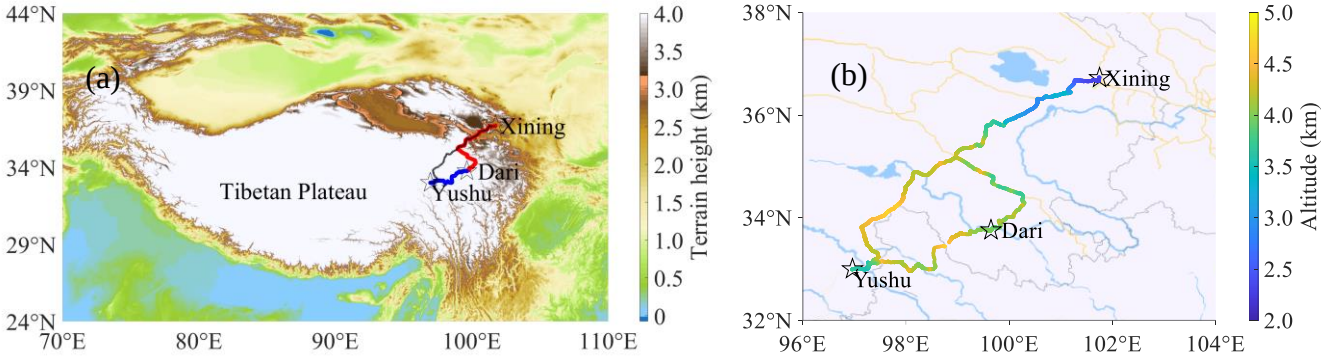


**Figure 2.** Driving routes of the mobile observation vehicle. The driving routes are added to **(a)** the terrain height map over the Tibetan Plateau (red, blue and black lines) and **(b)** the street map (https://map.baidu.com/, last access: 16 June 2022) in the experiment region as an overlay, respectively. The altitudes along the driving routes are marked by coloured dotted curves in figure (b). Light blue lines and areas in figure (b) indicate rivers and lakes.

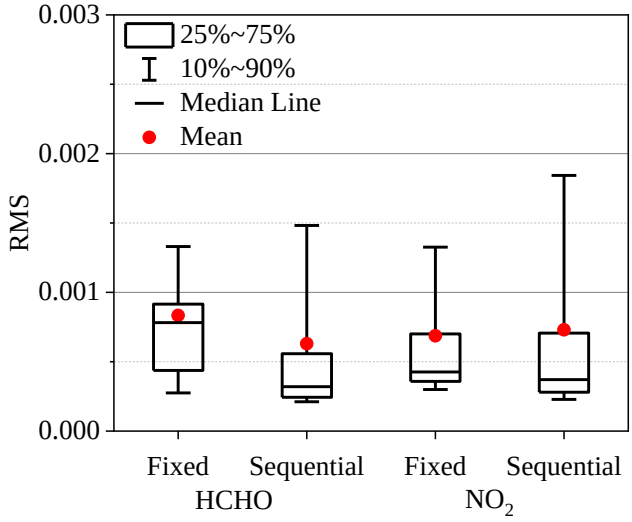


**Figure 3.** Statistics of the root mean square (RMS) of the $NO_2$ and HCHO spectral fitting residuals using a sequential FRS or fixed FRS (for RMS<0.005 and SZA<80 °) during the field campaign. Lower (upper) error bars and boxes are the 10th (90th), 25th (75th) percentiles, respectively. Lines inside the boxes and dots denote the medians and the mean values.

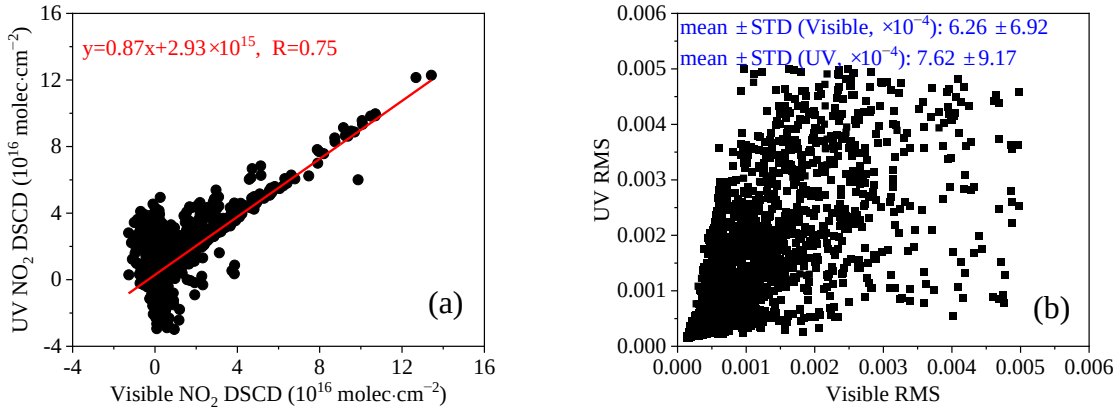


**Figure 4.** Comparison of $NO_2$ spectral fitting results using the visible and UV wavelength intervals (for RMS<0.005 and SZA<80 °) during the field campaign. **(a)** Linear fit of corresponding $NO_2$ DSCDs between visible and UV spectral intervals. **(b)** Corresponding $NO_2$ RMS between visible and UV spectral intervals. The red lines denote the results of the regression analyses and the corresponding equations and correlation coefficients are displayed in the figure (a). The numbers in figure (b) indicate the mean ± standard deviation (STD) in the visible and UV spectral intervals.

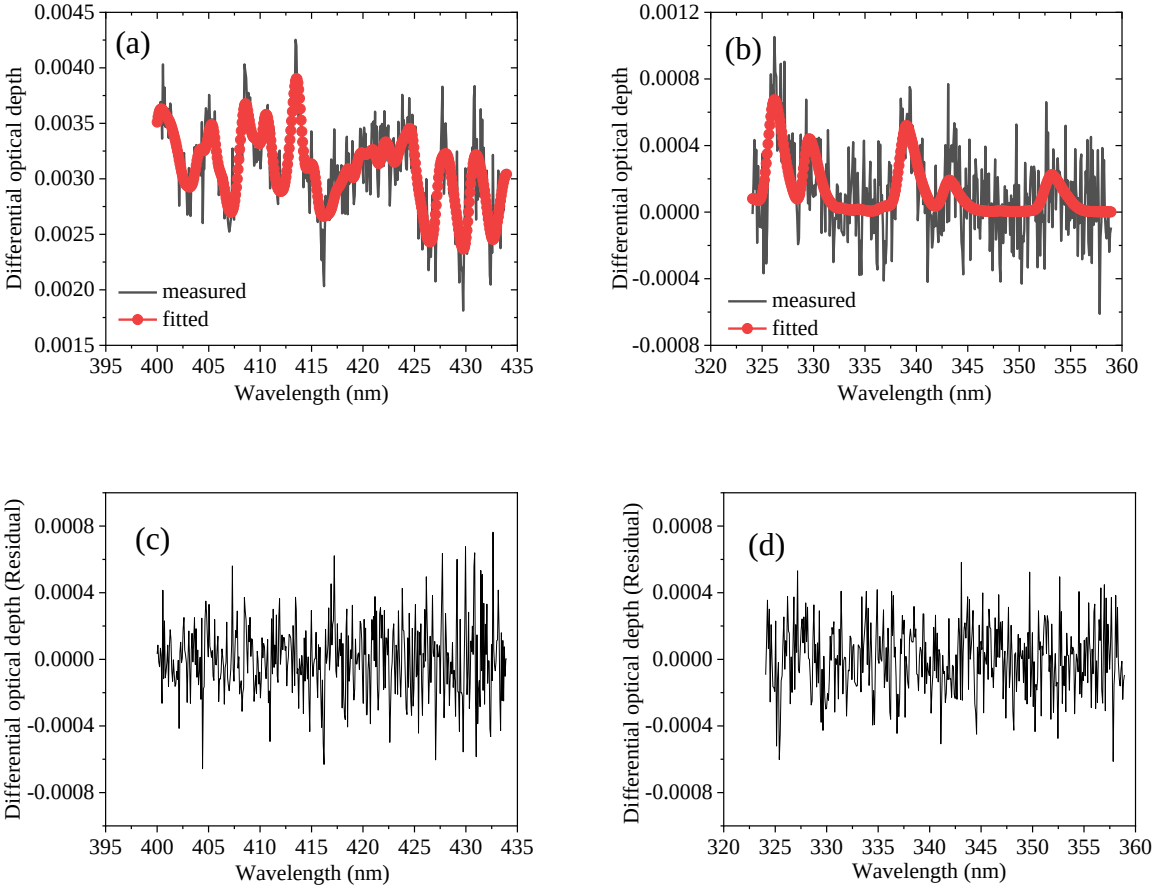


**Figure 5.** Examples of DOAS spectral analyses for $NO_2$ and HCHO. Black curves and red curves with dots indicate the measured and fitted differential optical depth for **(a)** $NO_2$ and **(b)** HCHO, respectively. The $NO_2$ and HCHO DSCDs are $5.27 \times 10^{15}$ molec $cm^{-2}$ and $9.36 \times 10^{15}$ molec $cm^{-2}$, respectively. The RMSs of the spectral fitting residuals between measured and fitted spectra are $2.17 \times 10^{-4}$ for **(c)** $NO_2$ and $2.09 \times 10^{-4}$ for **(d)** HCHO, respectively.

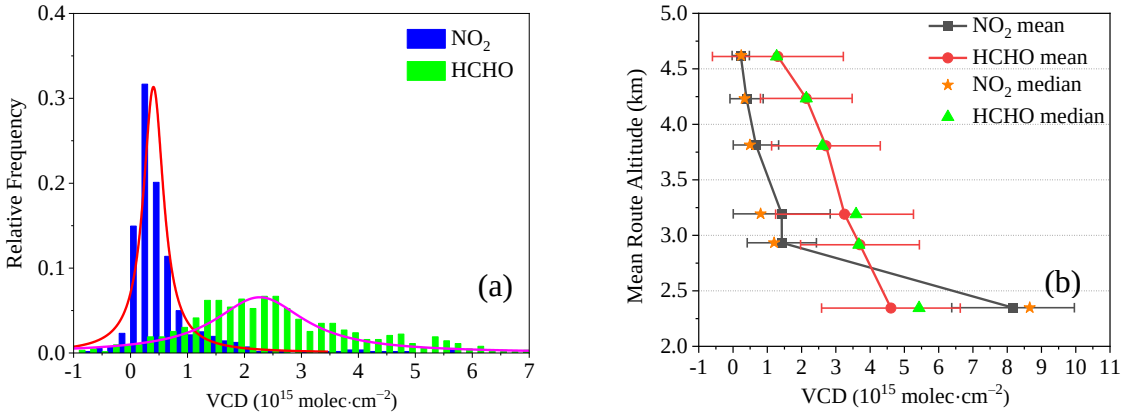


**Figure 6.** Overall characteristics of $NO_2$ and HCHO VCDs during the field campaign. **(a)** Frequency distributions of $NO_2$ (blue column) and HCHO (green column) VCDs as well as their Lorentz distribution curves for $NO_2$ (red curve) and HCHO (magenta curve), respectively. **(b)** Dependence of the $NO_2$ and HCHO VCDs on mean altitude of driving route from 2000 m to 5000 m at vertical intervals of 500 m. The black (red) lines with squares (dots), stars (triangles) and error bars denote the means, medians and standard deviations of the $NO_2$ (HCHO) VCDs for each altitude range.

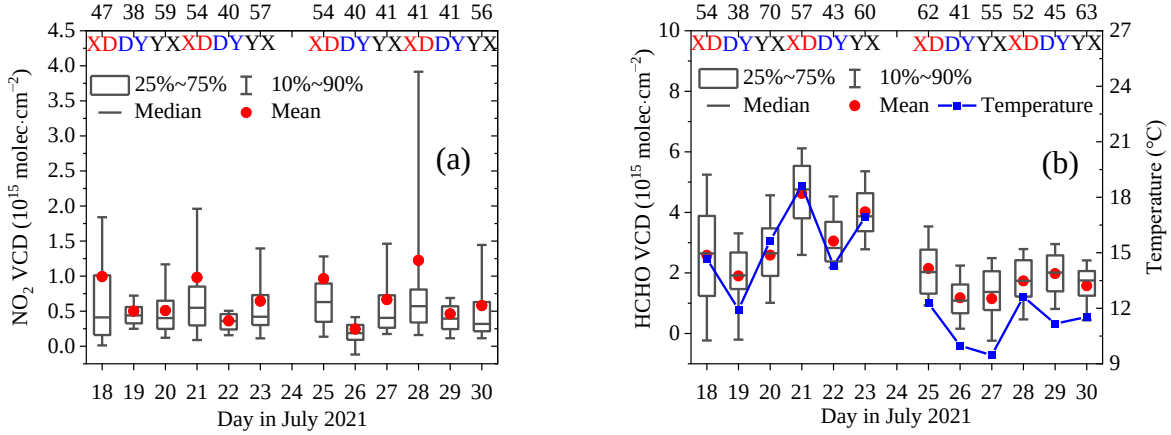


**Figure 7.** Day-to-day variations of the daily averaged **(a)** $NO_2$ and **(b)** HCHO VCDs over the mobile observation routes (XD, DY, YX). Lower (upper) error bars and boxes are the 10th (90th), 25th (75th) percentiles of the data. Lines inside the boxes and red dots denote the medians and the mean values, respectively. The integrated sampling numbers for specific day are labelled at the top axis. The blue curves with squares in Figure (b) denote the daily air temperature at 2 m above the land surface.

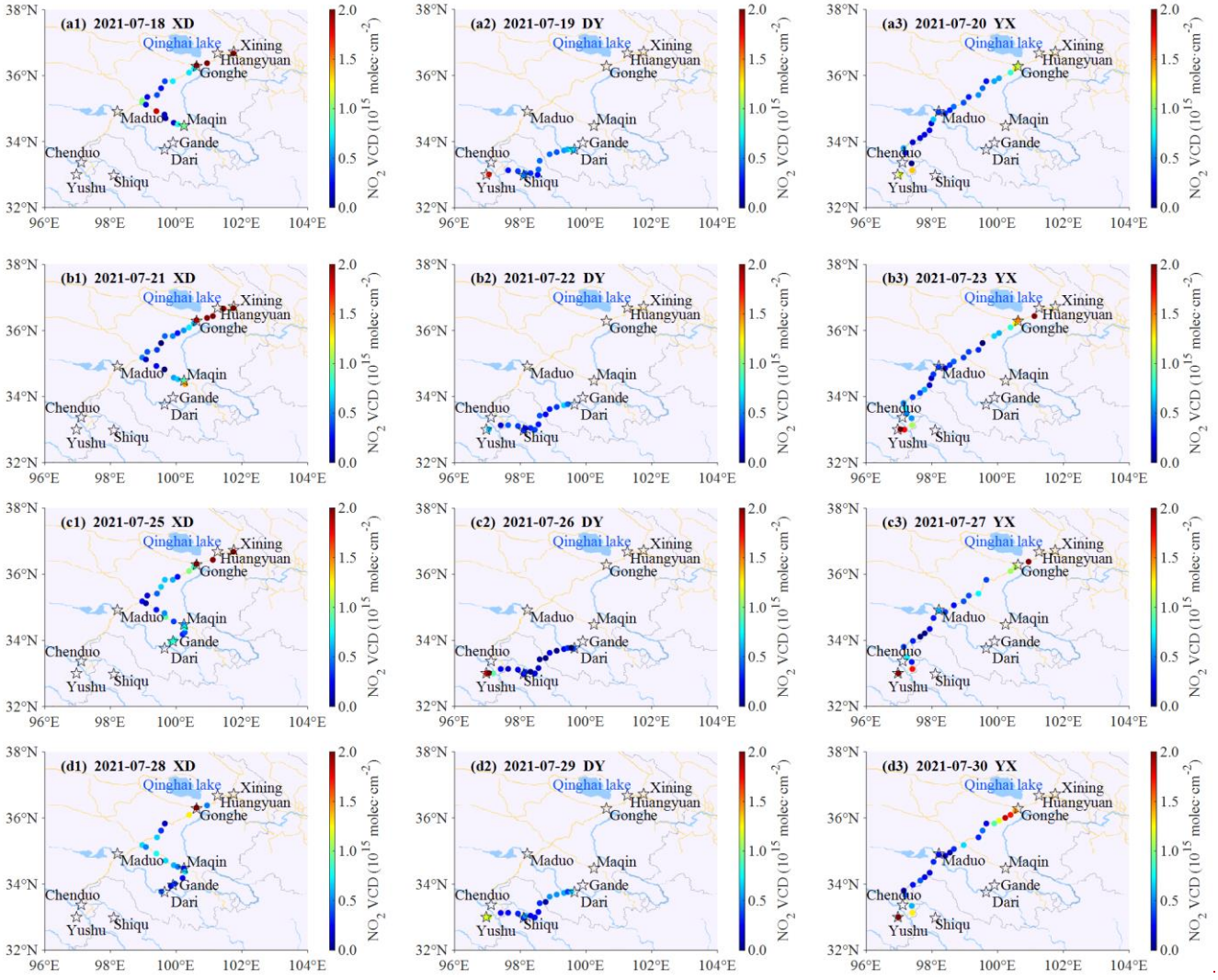
(a1) 2021-07-18 XD
(a2) 2021-07-19 DY
(a3) 2021-07-20 YX
(b1) 2021-07-21 XD
(b2) 2021-07-22 DY
(b3) 2021-07-23 YX
(c1) 2021-07-25 XD
(c2) 2021-07-26 DY
(c3) 2021-07-27 YX
(d1) 2021-07-28 XD
(d2) 2021-07-29 DY
(d3) 2021-07-30 YX
Qinghai lake
Xining
Huangyuan
Gonghe
Maduo
Maqin
Gande
Dari
Chenduo
Yushu
Shiqu
38°N
36°N
34°N
32°N
96°E
98°E
100°E
102°E
104°E
NO2 VCD (10^15 molec·cm^-2)
2.0
1.5
1.0
0.5
0.0

820

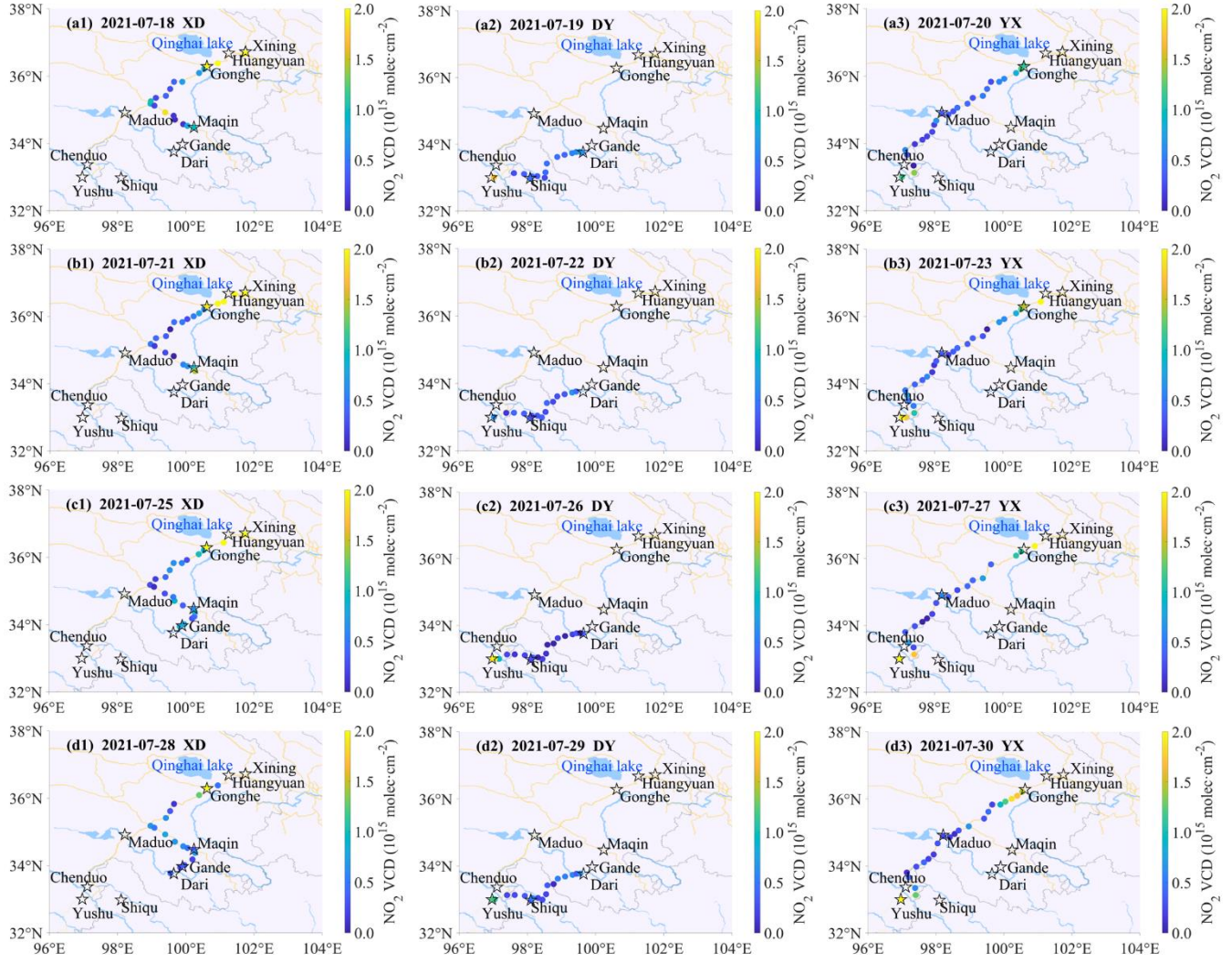


**Figure 8.** Spatial distributions of gridded $NO_2$ VCDs with 0.25 °×0.25 ° resolution. The observed $NO_2$ VCDs in each spatial grid cell are averaged for three segments **(1, 2, 3)** of four circling journeys **(a, b, c, d)**. The main cities and counties on the driving routes are marked by the black stars. On the background map, the light blue lines and areas represent rivers and lakes (such as, Qinghai Lake), the yellow lines denote the roads, and the grey lines indicate the administrative boundaries.

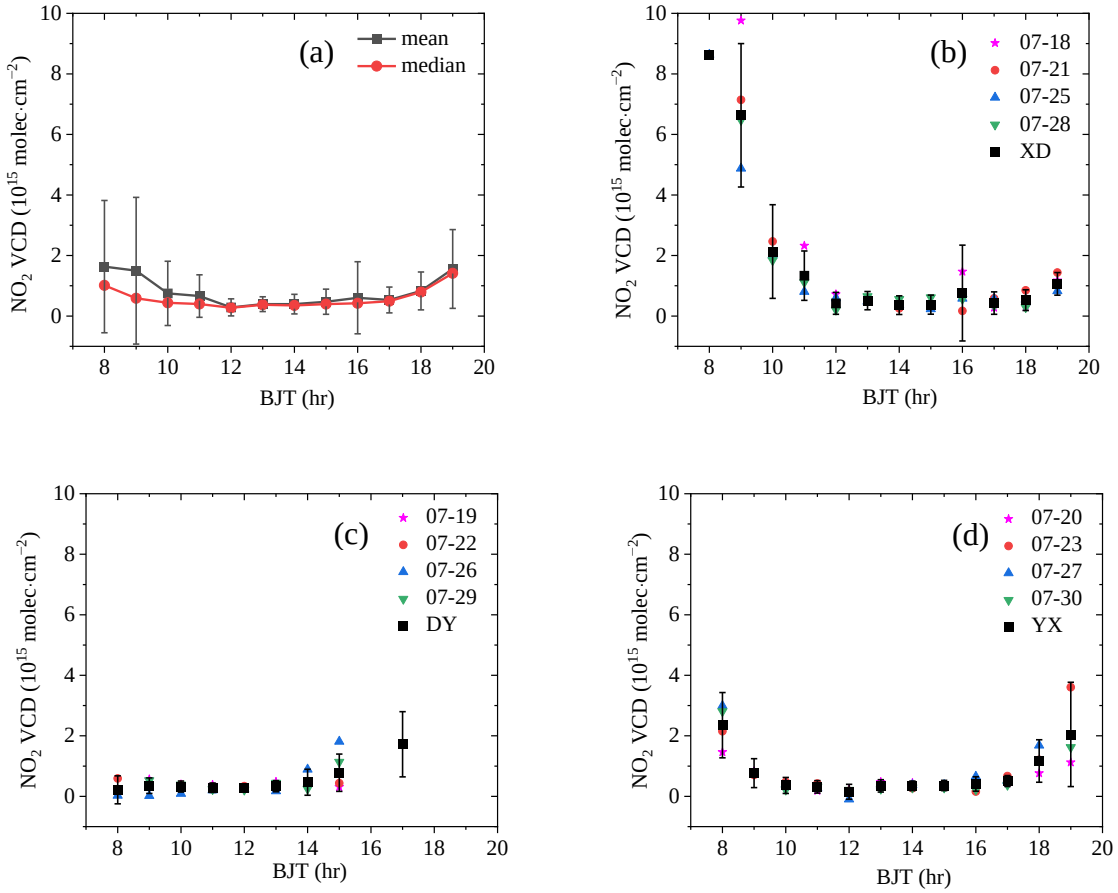


**Figure 9.** Diurnal variations of the $NO_2$ VCDs over the mobile observation routes. **(a)** Diurnal variations of the overall means (black curve with squares), medians (red curves with dots), and standard deviations (error bars) of the $NO_2$ VCDs. **(b)** Diurnal variations of the mean $NO_2$ VCDs on selected days (18/21/25/28 July 2021) as well as the means and standard deviations of the $NO_2$ VCDs on the XD driving route. **(c, d)** Same as (b), but for the DY and YX driving routes during the field campaign.

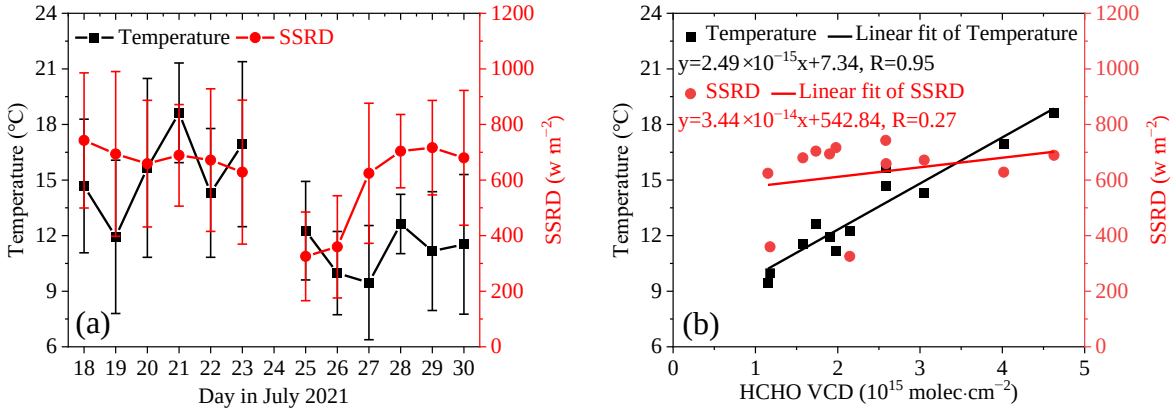


**Figure 10.** Comparison of the HCHO VCDs with other data sets. **(a)** Day-to-day variations of the mean air temperature at 2 m above the land surface (black curves with squares) and the downward solar radiation at the surface (SSRD, red curves with dots) as well as **(b)** linear fits between the two parameters and the daily averaged HCHO VCDs over the mobile observation routes. The error bars denote the standard deviations of the air temperature and SSRD in figure (a). The lines denote the results of the regression analyses, and the corresponding equations and correlation coefficients are displayed in the figure (b).

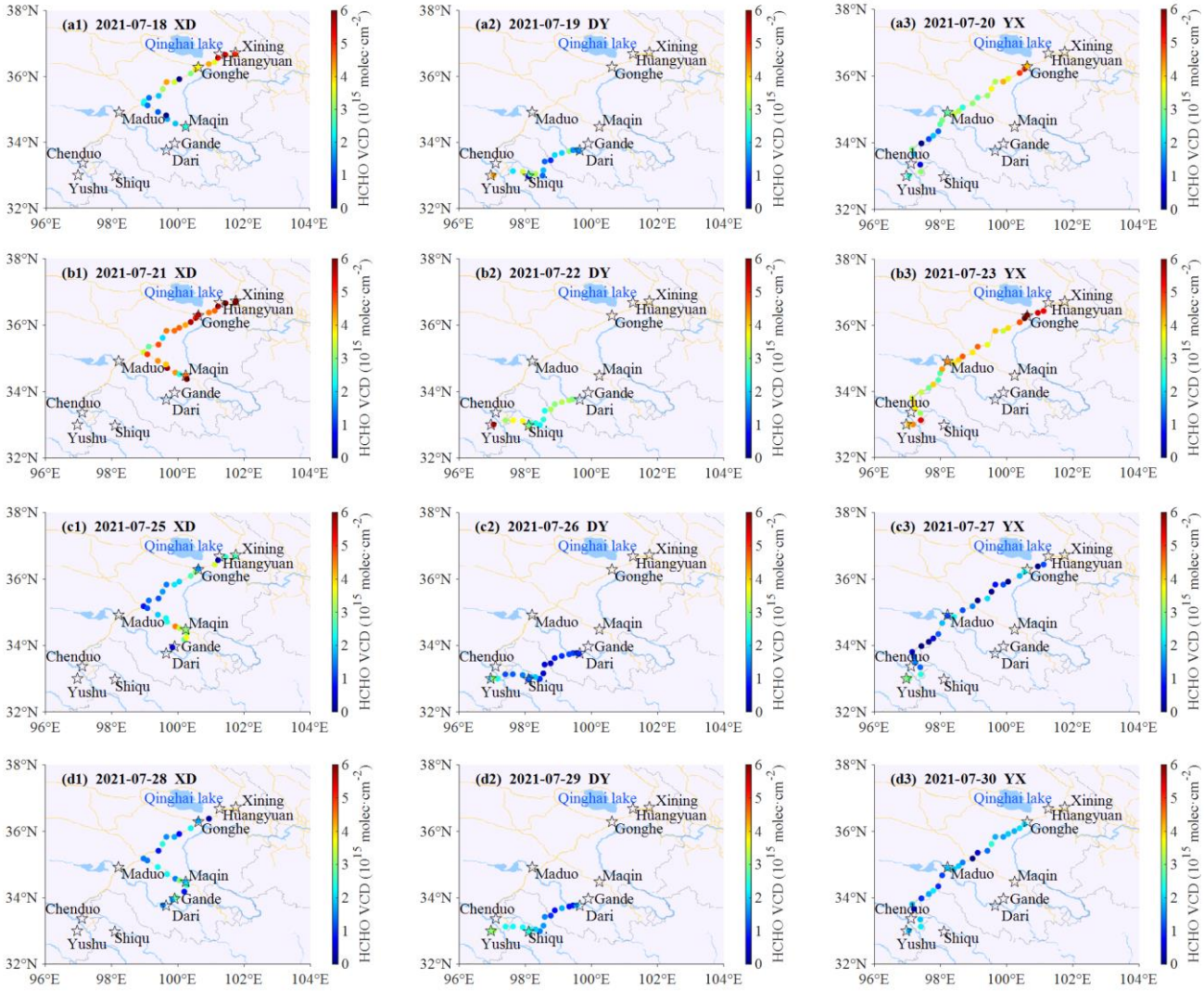
(a1) 2021-07-18 XD
(a2) 2021-07-19 DY
(a3) 2021-07-20 YX
(b1) 2021-07-21 XD
(b2) 2021-07-22 DY
(b3) 2021-07-23 YX
(c1) 2021-07-25 XD
(c2) 2021-07-26 DY
(c3) 2021-07-27 YX
(d1) 2021-07-28 XD
(d2) 2021-07-29 DY
(d3) 2021-07-30 YX
Qinghai lake
Xining
Huangyuan
Gonghe
Maduo
Maqin
Gande
Dari
Chenduo
Yushu
Shiqu
38°N
36°N
34°N
32°N
96°E
98°E
100°E
102°E
104°E
HCHO VCD ($10^{15}$ molec·cm$^{-2}$)
0
1
2
3
4
5
6

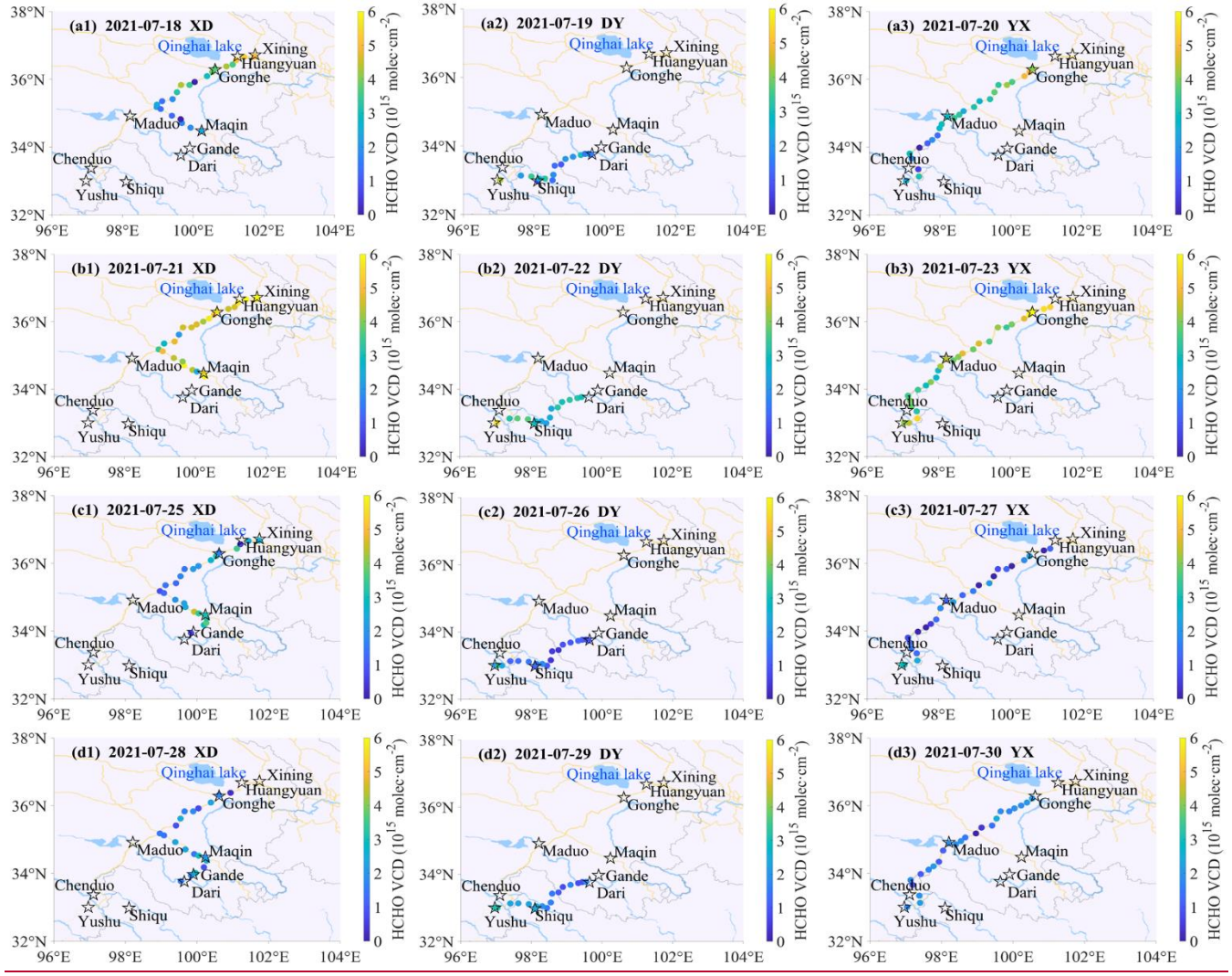


840 **Figure 11.** Same as figure 8, but for HCHO.

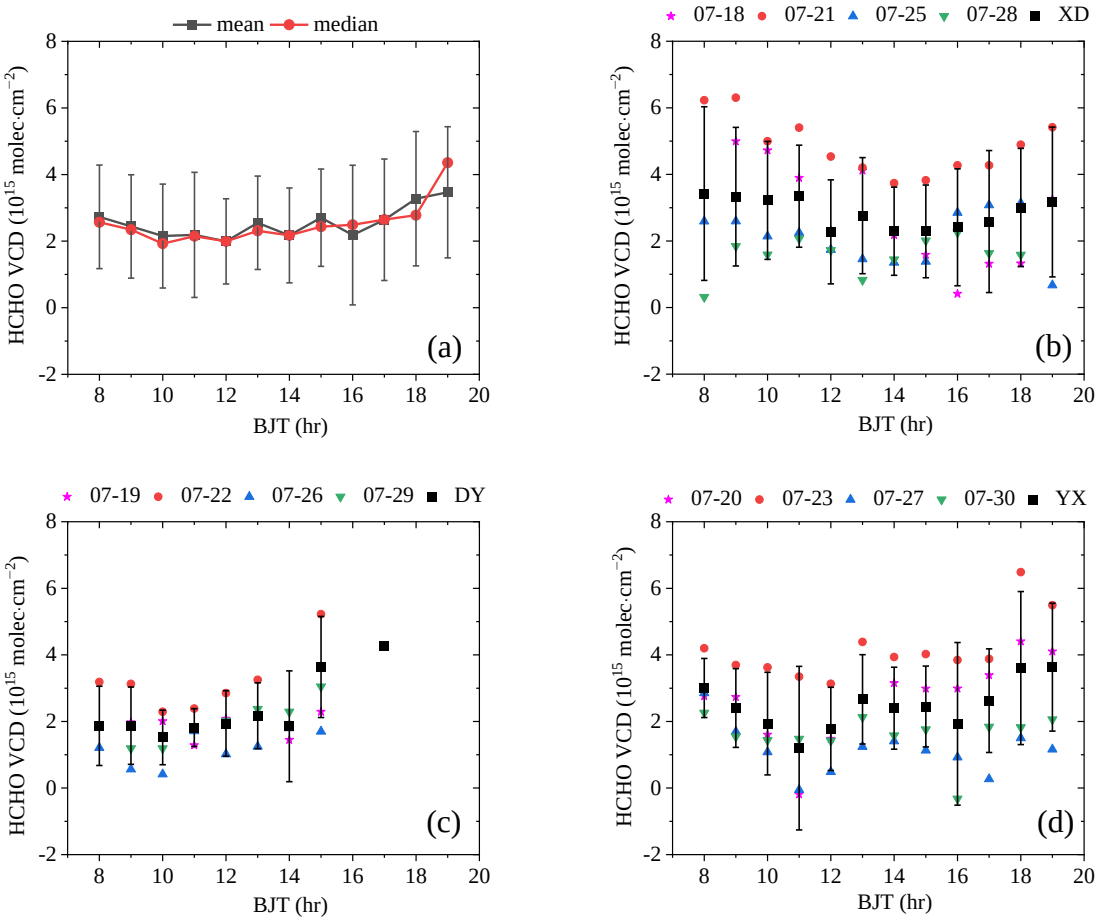


**Figure 12.** Same as figure 9, but for HCHO.

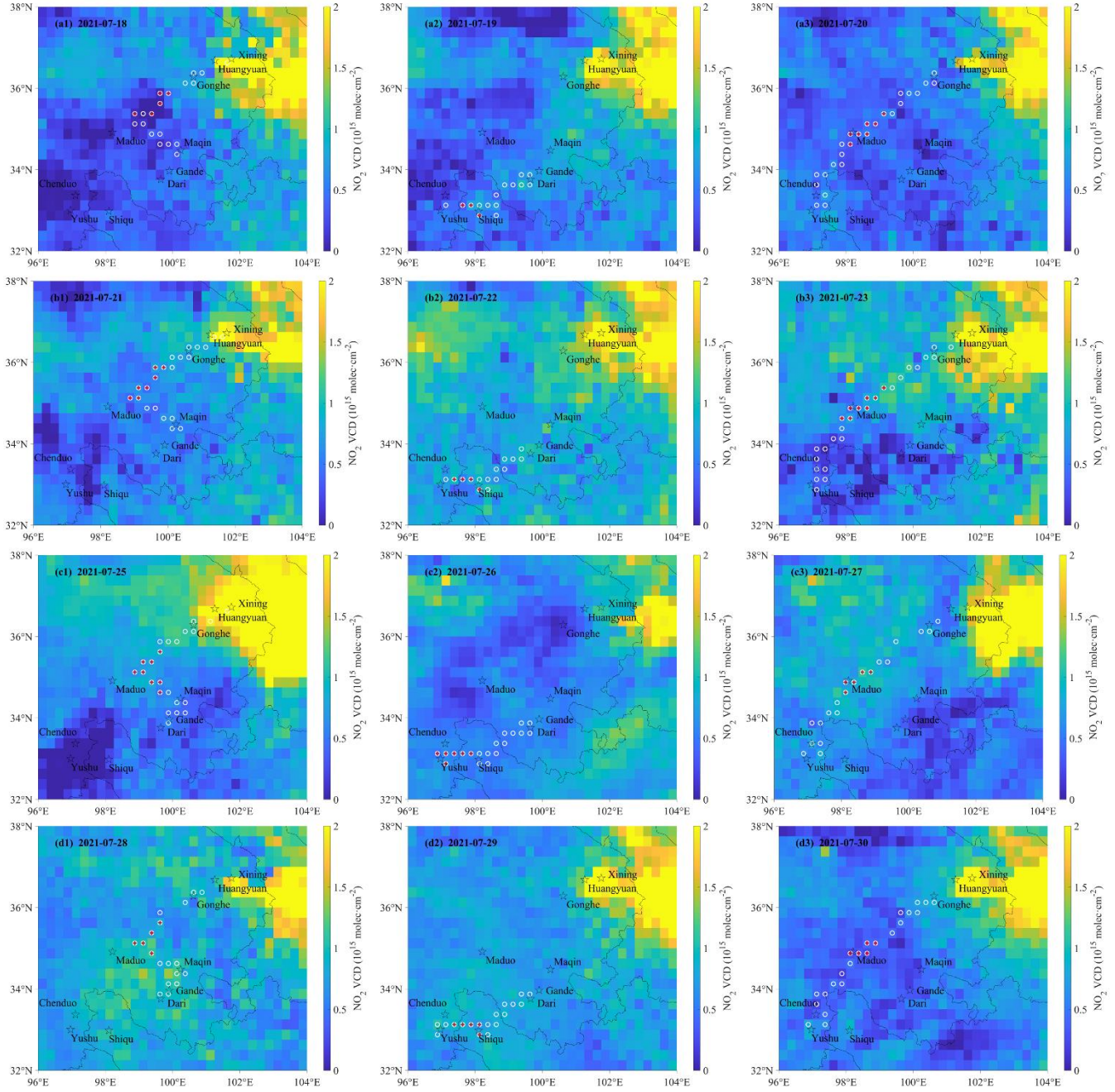


845 **Figure 13.** Spatial distributions of the tropospheric $NO_2$ VCDs observed by TROPOMI on each day of the field campaign. The TROPOMI S5P_L2__NO2____HiR product has been gridded to 0.25 °×0.25 ° cells. The main cities and counties on the driving routes of the field campaign are marked by the black stars. The black curves indicate the administrative boundaries. The white circles and red plus symbols show the grid cell where the data of both TROPOMI and MAX-DOAS are available on the same day or within a 1.5 h time difference, respectively.

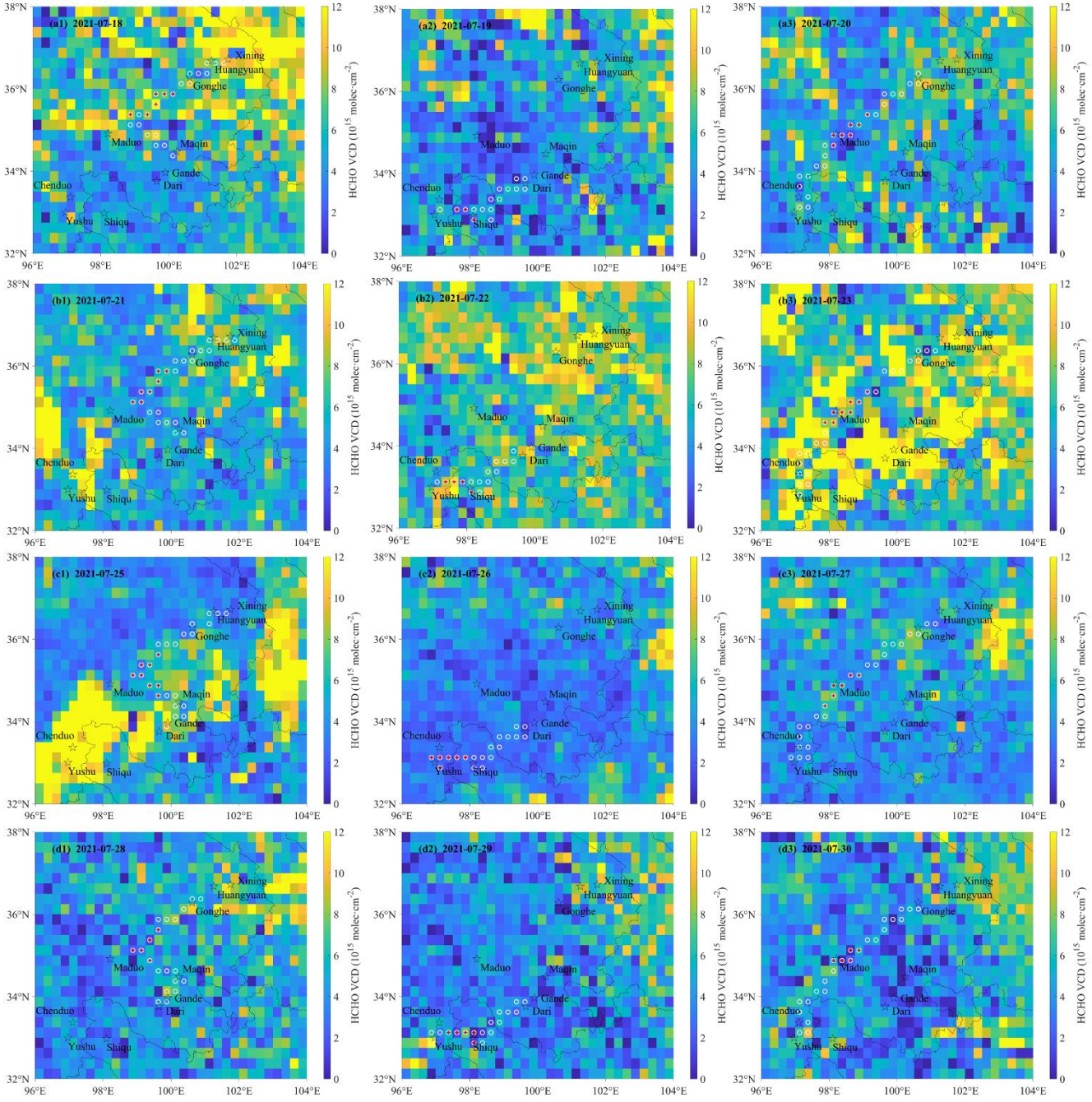


**Figure 14.** Same as figure 13, but for HCHO.

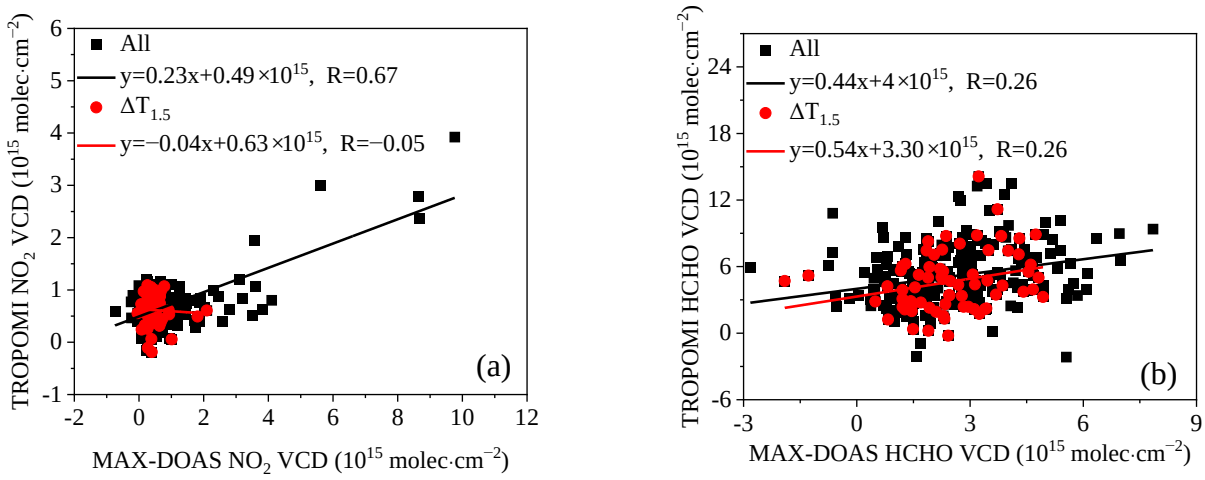


**Figure 15.** Linear fit between the tropospheric **(a)** $NO_2$ and **(b)** HCHO VCDs measured by the mobile MAX-DOAS and TROPOMI. The black squares and red dots represent the available VCDs of both data sets at the same grid cell on the same day or within a 1.5 h time difference, respectively. The black (red) lines denote the results of the regression analyses and the corresponding equations and correlation coefficients are displayed in the figures.